Materials & Design 257 (2025) 114375

Contents lists available at ScienceDirect

Materials & Design

journal homepage: www.elsevier.com/locate/matdes

Atomic layer deposition of SnO_2 and TiO_2 on electrodeposited BiOI thin films for efficient light-driven peroxymonosulfate activation

Laura Huidobro [a,b], Mahmoud Abid [c], Haitham Maslouh [c], Arnaud Demore [c], Mikhael Bechelany [c,d], Elvira Gómez [a,b], Albert Serrà [a,b,*]

[a] Grup d'Electrodeposició de Capes Primes i Nanoestructures (GE-CPN), Departament de Ciència de Materials i Química Física, Universitat de Barcelona, Martí i Franquès, 1, Barcelona E-08028 Catalonia, Spain
[b] Institute of Nanoscience and Nanotechnology (IN^{2}UB), Universitat de Barcelona, Barcelona, Catalonia, Spain
[c] Institut Européen des Membranes, IEM, UMR 5635, University of Montpellier, ENSCM, CNRS, Montpellier, France
[d] Functional Materials Group, Gulf University for Science and Technology (GUST), Mubarak Al-Abdullah 32093, Kuwait

ARTICLE INFO

Keywords:
Photocatalysis
Peroxymonosulfate activation
Heterojunction thin films
Water decontamination
Advanced oxidation processes

ABSTRACT

Light-driven peroxymonosulfate (PMS) activation is gaining traction as a green advanced oxidation strategy for degrading recalcitrant water pollutants; however, catalyst instability and sluggish charge separation still hinder its practical application. Here, we report for the first time the fabrication of ALD-engineered BiOI thin-film heterojunctions, coated with nanometric SnO_2 or TiO_2 layers (~5 nm) and decorated with Pd nanoparticles (~2 nm), which simultaneously enhance catalytic activity and stability. The BiOI/SnO_2 and BiOI/TiO_2 systems exhibit well-defined type-II band alignments, facilitating efficient interfacial charge transfer, while Pd nanoparticles form Schottky junctions that extract photogenerated electrons and mitigate BiOI photocorrosion. Using 20 ppm tetracycline (TC) at pH 7 as a model contaminant, TiO_2-BiOI achieved 92.7 % TC removal and 84.8 % total organic carbon (TOC) mineralization within 90 min under UV-A light (365 nm) with 2.5 mM PMS. In contrast, SnO_2-BiOI showed superior performance under simulated sunlight ($\lambda > 400$ nm), attaining 80.8 % degradation and 76.5 % mineralization. Radical scavenging assays revealed a threefold increase in sulfate and hydroxyl radical production compared to pristine BiOI. Pd modification reduced Bi and I leaching by more than 80 % after 360 min of continuous irradiation and preserved over 95 % of the photocatalytic activity across ten successive reuse cycles. This work establishes a modular ALD-based strategy to design stable semiconductor/oxide/metal nanointerfaces for wavelength-tunable PMS activation. The resulting thin-film catalysts, fabricated on FTO substrates with sub-nanometer precision, offer a scalable platform for solar-driven water purification and expand the material design space for sulfate-radical-based advanced oxidation processes.

1. Introduction

Water quality deterioration – driven by the continuous discharge of industrial effluents, pharmaceutical residues, pesticides, and heavy metal complexes – has become one of the most urgent environmental challenges of our time [1–4]. Conventional treatment methods such as coagulation–filtration, adsorption, and biological oxidation often merely transfer contaminants from one phase to another and struggle when confronted with chemically persistent or structurally diverse pollutants [5–8]. Advanced oxidation processes (AOPs), which generate highly reactive oxygen or sulfate radicals in situ, significantly more powerful alternative: they can mineralize a wide spectrum of compounds to CO_2 and H_2O at near-neutral pH and with relatively modest energy inputs [9–13].

Among emerging AOP strategies, peroxymonosulfate (PMS, HSO_5^-) has gained considerable attention due to its high redox potential (2.6–3.1 V) and manifold activation pathways [7,14–18]. Four principal activation routes have been identified: (i) sonochemistry, where acoustic cavitation cleaves the O–O bond in PMS but suffers from low energy-conversion efficiency and scale-up challenges; (ii) electrochemical activation on boron-doped diamond or MXene electrodes, which achieves high faradaic efficiency yet contends with electrode

* Corresponding author at: Grup d'Electrodeposició de Capes Primes i Nanoestructures (GE-CPN), Departament de Ciència de Materials i Química Física, Universitat de Barcelona, Martí i Franquès, 1, Barcelona E-08028, Catalonia, Spain.
E-mail address: a.serra@ub.edu (A. Serrà).

https://doi.org/10.1016/j.matdes.2025.114375
Received 12 June 2025; Received in revised form 7 July 2025; Accepted 10 July 2025
Available online 10 July 2025

passivation and costly cell designs; (iii) non-radical PMS activation by carbonaceous materials—nitrogen-doped graphene or carbon nanotube aerogels—whose singlet-oxygen pathways avoid metal leaching but rely on powder catalysts that complicate separation; and (iv) semiconductor-assisted photocatalysis, which pairs solar energy harvesting with benign operation, yet often requires ultraviolet (UV) light (e.g., TiO_2, ZnO) or contends with rapid electron–hole recombination and structural instability under visible irradiation [19–26].

Within this context, bismuth oxyiodide (BiOI) has emerged as a promising photocatalyst for environmental remediation. BiOI, a p-type semiconductor, features a layered tetragonal structure that facilitates efficient charge separation and exhibits a narrow bandgap (~1.8–2.0 eV), allowing visible-light-driven photocatalysis [27,28]. However, BiOI faces significant drawbacks that limit its practical application in water treatment: (i) poor stability due to iodine leaching, leading to photocorrosion under prolonged irradiation; (ii) high electron–hole recombination rates, which reduce overall photocatalytic efficiency; and (iii) a valence band position that is not sufficiently positive to generate hydroxyl radicals ($^{\bullet}OH$), which are essential for the degradation of persistent pollutants [27,29–33].

To overcome these challenges, researchers have explored several strategies to enhance the stability and photocatalytic efficiency of BiOI. One effective approach is thermal treatment, which transforms BiOI into other bismuth oxyiodides (e.g., $Bi_4O_5I_2$, Bi_5O_7I, Bi_2O_4I, and Bi_2O_3) [27,31,34–37]. Another widely adopted strategy is the construction of heterojunctions with wide-bandgap semiconductors to enhance charge separation and suppress electron-hole recombination. TiO_2 and SnO_2 are particularly effective due to their suitable conduction band positions, facilitating electron transfer from BiOI and promoting reactive species generation [28,38–41]. By strategically aligning the conduction and valence bands of BiOI with those of a secondary semiconductor, charge carriers can be efficiently transferred across the interface, thereby extending their lifetimes and enhancing reactive species generation for pollutant degradation. The use of atomic layer deposition (ALD) further enhances heterojunction performance by providing sub-nanometer control over film thickness, excellent conformality, and defect-free interfaces, all critical for optimizing interfacial charge transfer [42–45].

In addition, doping or decorating BiOI with noble metals such as Pd, Au, and Ag has proven to be effective in enhancing electron mobility and promoting surface plasmon resonance effects [46]. These metals act as electron sinks, reducing charge recombination and increasing the efficiency of light absorption, particularly in the visible-light range. In this context, the deposition of Pd nanoparticles by ALD offers additional advantages, providing precise control over nanoparticle size, distribution, and interfacial contact, which are critical for maximizing electron trapping and plasmonic effects. Another highly effective strategy involves combining photocatalysis with PMS activation, which facilitates the formation of reactive sulfate radicals ($SO_4^{\bullet-}$). By implementing these modifications, BiOI-based photocatalysts demonstrated improved efficiency, stability, and reusability, making them more viable for real-world water purification applications [47–51].

To boost BiOI-mediated pollutant degradation and mineralization, we tailor the material's architecture to enlarge its active surface, enhance light harvesting, and suppress electron–hole recombination [31,52]. Here, electrodeposited BiOI thin films are conformally coated by ALD with nanometric shells of SnO_2 or TiO_2 and, in a second step, decorated with Pd nanoparticles. The wide-band-gap oxides extend light absorption and promote charge separation, whereas the Pd nanodots act as electron sinks, improving surface reactivity [53–56]. We then couple the resulting heterojunctions with PMS to study visible light mineralization of antibiotics in water. The simultaneous investigation of BiOI/SnO_2 and BiOI/TiO_2 heterostructures allows for a direct comparison of how differences in band alignment, charge transport dynamics, and ALD oxide characteristics influence ROS generation and photocatalytic efficiency. This comparison under identical experimental conditions provides valuable insight into the structure–performance relationships governing PMS-activated degradation. Furthermore, this study explores the synergistic effect of photocatalysis and PMS activation on the degradation and mineralization of antibiotics in water. To the best of our knowledge, this is the first time that ALD-engineered TiO_2- and SnO_2-BiOI heterojunctions, further modified with Pd nanoparticles, have been applied for light-driven PMS-activated degradation and mineralization of pollutants. The synergistic integration of ALD-designed heterojunctions with PMS activation under both UV and visible light irradiation offers a novel and effective approach for antibiotic removal.

2. Materials and methods

2.1. Materials

Bismuth nitrate pentahydrate ($Bi(NO_3)_3{\cdot}5H_2O$, ≥98 %; CAS: 10035-06-0), potassium iodide (KI, ≥99 %; CAS: 7681-11-0), p-benzoquinone (≥98 %; CAS: 106-51-4), sodium hydroxide (NaOH, ≥97 %; CAS: 1310-73-2), sodium bromide (NaBr, ≥99.5 %; CAS: 7647-15-6), tetrakis (dimethylamino)tin(IV) (TDMASn, ≥99.99 %; CAS: 1066-77-9), tetrakis (dimethylamino)titanium(IV) (TDMAT, ≥99.99 %; CAS: 1066-77-9), palladium(II) hexafluoroacetylacetonate ($Pd(hfac)_2$, 99.9 %; CAS:64916-48-9), formalin solution (37 wt% formaldehyde stabilized with methanol; CAS:50-00-0), nitric acid (HNO_3, 65 %; CAS: 7697-37-2), sodium terephthalate (Na_2TPA; CAS: 10028-70-3), bromine (Br_2; CAS: 7726-95-6), and OXONE® (peroxymonosulfate, PMS, ≥98 %; CAS: 104548-30-3) were obtained from Sigma-Aldrich, Panreac, Fischer Chemical, Alfa Aesar, Strem Chemicals, or Thermo Scientific Chemicals and used without further purification. Tetracycline hydrochloride (TC, ≥98 %, CAS: 60-54-8), levofloxacin (LEV, ≥98 %, CAS: 100986-85-4), and lansoprazole (LAN, >98 %, CAS: 103577–45-3) were purchased from Merck and Alfa Aesar. All aqueous solutions were prepared using Milli-Q ultrapure water (18.2 MΩ·cm). Fluorine-doped tin oxide (FTO) glass substrates (2.2 mm thickness, ~7 Ω/sq) were supplied by Sigma-Aldrich. Argon (5.0 purity) was obtained from Linde and used as a carrier and purge gas during the ALD processes. Tap water was sourced from the Chemistry School facilities at the University of Barcelona, pre-filtered using a 0.5 μm membrane to remove suspended solids, and subsequently used for the catalytic experiments. The water presented moderate buffering capacity, characterized by an alkalinity of 166 mg $CaCO_3$ L^{-1}, and a slightly basic pH of 7.75. Total hardness was measured at 234 mg $CaCO_3$ L^{-1}, predominantly due to calcium (67.2 mg L^{-1}) and magnesium (16.6 mg L^{-1}) ions. The main dissolved salts were sodium (106 mg L^{-1}), chloride (175 mg L^{-1}), and sulfate (79.6 mg L^{-1}), with a total organic carbon (TOC) concentration of 4.9 ppm. For photocatalytic experiments, the pH was adjusted to 7.00 prior to use.

2.2. Synthesis and characterization of photocatalytic thin films

2.2.1. Electrochemical synthesis of BiOI thin film

BiOI thin films were electrodeposited using a three-electrode system connected to a potentiostat/galvanostat (Autolab PGSTAT30) controlled via NOVA software. The working electrode was fluorine-doped tin oxide (FTO) glass (2.2 mm thickness, ~7 Ω resistivity, Sigma-Aldrich) with an active area of 0.8 cm^2. A Pt wire served as the counter electrode, while an $Ag|AgCl|Cl^-$ (3 M) electrode was used as the reference. Electrodeposition was carried out at a previously optimized potential of −0.2 V vs. Ag/AgCl in an electrolytic solution containing bismuth nitrate, potassium iodide, nitric acid, and p-benzoquinone, using a 50:20 (v:v) water–ethanol medium. Specifications of electrochemical bath preparation and electrodeposition parameters were detailed in previous studies [27,31].

2.2.2. Deposition via atomic layer deposition (ALD)

Electrodeposited BiOI thin films, as previously described, were used as substrates for the subsequent deposition of SnO_2 and TiO_2 thin films by ALD. ALD enables the deposition of conformal and uniform thin films

with atomic-level control over thickness, making it particularly suitable for tailoring photocatalytic materials. The choice of SnO_2 and TiO_2 as coating materials on BiOI was based on their wide bandgaps, favorable conduction band alignment with BiOI, and their known ability to enhance charge separation and suppress recombination in heterojunction structures. Both oxides also exhibit excellent stability under irradiation and enable efficient transfer of photogenerated electrons from BiOI, which is essential for the activation of PMS into reactive sulfate radicals. Specifically, SnO_2 was selected for its superior electron mobility, which improves charge transport, while TiO_2 offers robust UV photoactivity. Their integration with BiOI was intended to optimize photocatalytic activity and increase film stability under light-driven PMS activation conditions. By varying the thickness of the SnO_2 and TiO_2 coatings, the photocatalytic performance of the BiOI-based films was systematically optimized for water treatment applications [57,58].

- Atomic layer deposition of tin oxide (SnO_2): SnO_2 thin films were deposited at 200 °C using a commercial ALD reactor (Savannah G2 S100, Cambridge NanoTech Inc) by employing tetrakis(dimethylamino)tin $[(CH_3)_2N]_4Sn$ and H_2O as precursors. Additionally, the thin films were carried out via successive ALD cycles. The tin precursor utilized was tetrakis(dimethylamino)tin(IV) (TDMASn, $[(CH_3)_2N]_4Sn$), while deionized water served as the oxidizing oxygen source. The depositions were conducted under a constant flow of 20 sccm of argon (5.0 purity, Linde) as the carrier gas, with a reactor temperature maintained at 200 °C. The TDMASn precursor was heated to 80 °C, while the water was kept at room temperature. The substrates were positioned in the reactor and held at 200 °C for a 20 min duration, during which a constant argon flow of 20 sccm was maintained. The deposition sequence consisted of a 0.1 s pulse of TDMASn, followed by a 20 s argon purge, a 0.035 s pulse of H_2O, and a final 20 s argon purge. The growth rate of the SnO_2 films reached a saturation point at approximately 0.5 Å/cycle. The thickness of the SnO_2 films was controlled by selecting the number of ALD cycles, with 20, 100, and 200 cycles resulting in film thicknesses of 1 nm, 5 nm, and 10 nm, respectively.
- Atomic layer deposition of titanium oxide (TiO_2): For TiO_2 deposition, the process was conducted using the same ALD system, with Tetrakis(dimethylamino)titanium(IV) (TDMAT) and H_2O as precursors. The chamber was maintained at 120 °C, and a constant flux of pure argon gas (20 sccm) was used to ensure an inert atmosphere. The titanium precursor bubbler was maintained at 75 °C to ensure sufficient vapor pressure for deposition. The deposition sequence for TiO_2 involved a 0.1 s pulse of TDMAT, followed by a 20 s argon purge, a 0.015 s pulse of H_2O, and a final 20 s argon purge. The growth rate of the TiO_2 films reached saturation at approximately 0.48 Å/cycle, enabling precise control over film thickness with excellent reproducibility. The thickness of the TiO_2 films was controlled by varying the number of ALD cycles, with 21, 105, and 210 cycles resulting in film thicknesses of ~1 nm, ~5 nm, and ~10 nm, respectively
- Atomic layer deposition of palladium (Pd): To enhance the catalytic efficiency of SnO_2-BiOI and TiO_2-BiOI, Pd nanoparticles were synthesized by ALD in a low-pressure hot-wall reactor (home-built) as described in previous Works [57,59]. ALD of Pd was carried out using palladium(II) hexafluoroacetylacetonate ($Pd(hfac)_2$) as the precursor and formalin as the reducing agent. To synthesize highly dispersed Pd nanoparticles, 100 ALD cycles were applied. The bubbler containing the $Pd(hfac)_2$ precursor was heated to 70 °C, while the formalin container was kept at room temperature. The deposition chamber was maintained at 220 °C, and the lines of the ALD system were heated to 80 °C to prevent any condensation. The ALD cycle consisted of sequential pulses, exposures, and purges of Pd precursor and formalin. For $Pd(hfac)_2$, the pulse, exposure, and purge durations were 5 s, 60 s, and 10 s, respectively, while for formalin, the durations were 1 s, 60 s, and 60 s, respectively.

2.2.3. Materials characterization

The surface morphology of the synthesized samples was analyzed using field emission scanning electron microscopy (FE-SEM, JEOL J-7100), equipped with an energy-dispersive X-ray spectroscopy (EDX) detector for elemental analysis. To evaluate the light transmission through the ALD coatings, optical power measurements were conducted under UV-A (365 nm) and visible-light sources. Samples were prepared on FTO substrates with: (i) 5 nm SnO_2, (ii) 5 nm TiO_2, (iii) 5 nm SnO_2 + 1 nm Pd, and (iv) 5 nm TiO_2 + 1 nm Pd. A calibrated photodetector (Thorlabs PM100D with S120C head) was positioned behind each sample and the incident power was normalized to that of bare FTO. The chemical nature of the samples was determined using X-ray photoelectron spectroscopy (XPS) with an ESCALAB 250 spectrometer (Thermo Electron) and an Al Kα monochromatic source (1486.6 eV) for excitation. The crystalline phase was analyzed using a Panalytical X'Pert Pro diffractometer with Cu Kα radiation. Photoluminescence (PL) spectra were recorded using a custom-built setup consisting of a 365 nm LED excitation source (M365FP1, Thorlabs), bandpass-filtered with a 360 ± 5 nm filter (FB360-10, Thorlabs). The backscattered PL emission was collected through a long-pass filter (cutoff at 400 nm; FEL0400, Thorlabs) and analyzed using an Andor 193i spectrometer coupled with an Andor iDus CCD camera.

2.3. Study of degradation and mineralization of organic pollutants

To assess the catalytic efficiency of the synthesized materials, a comprehensive study was conducted on the degradation and mineralization of TC solutions. Experiments were performed in a 20 ppm TC solution at pH 7 under various conditions: visible-light irradiation, UV-light irradiation, the presence of PMS, and their combinations. In each experiment, a sample of the corresponding deposited catalyst was introduced into 3 mL of the TC solution. Prior to the catalytic study, all samples were immersed in the TC solution under dark conditions for 30 min to establish adsorption–desorption equilibrium.

For experiments involving PMS, 30 μL of a freshly prepared concentrated PMS solution was added to the 3 mL TC solution, resulting in a final PMS concentration of 2.5 mM. Visible-light irradiation experiments were conducted using a 1.6 W white LED strip (2.2×10^{-3} W cm^{-2}), while UV-light experiments were carried out using a UV-A source ($\lambda = 365$ nm, Darkbeam® flashlight) with an intensity of 1.6×10^{-3} W cm^{-2}.

TC degradation was monitored by measuring the solution's absorbance at regular intervals over a 90-minute period using a UV–vis spectrophotometer (Shimadzu UV-1800). For the mineralization study, total organic carbon (TOC) content was analyzed using high-temperature combustion analysis (TOC-VCSH, Shimadzu).

To investigate the contribution of individual reactive species, radical trapping experiments were carried out using the following scavengers: benzoquinone (BQ, 1 mM) for superoxide radicals ($O_2^{\bullet-}$), methanol (MeOH, 1 mM) for both hydroxyl ($^{\bullet}OH$) and sulfate radicals ($SO_4^{\bullet-}$), *tert*-butyl alcohol (TBA, 1 mM) for $^{\bullet}OH$ radicals, and disodium ethylenediaminetetraacetate (EDTA, 1 mM) for photogenerated holes (h^+). Scavengers were added to the TC solution prior to light irradiation, and the change in photocatalytic performance was monitored under both UV-A and visible light conditions.

To elucidate the degradation pathway of TC, high-performance liquid chromatography coupled with mass spectrometry (HPLC-MS) analysis was performed after photocatalytic reactions using 5 nm SnO_2-BiOI and 5 nm TiO_2-BiOI samples with PMS under UV-A and visible light. The residual solution was filtered and analyzed using a Waters Alliance 2695 HPLC system coupled to a ZQ 2000 mass detector in positive ESI mode. A reversed-phase C18 column (150 × 4.6 mm, 5 μm) was used with a gradient mobile phase of water (0.1 % formic acid) and acetonitrile. The flow rate was 0.5 mL·min^{-1}. Mass spectra were recorded in the range *m/z* 50–500. Intermediate products were identified based on their *m/z* values, and proposed transformation pathways

were constructed based on chemical logic and prior literature.

To further evaluate the catalysts' effectiveness against other contaminants, additional mineralization studies were conducted using two single-pollutant solutions: 20 ppm LEV, and 5 ppm LAN. Additionally, multipollutant (MP) solutions containing 5 ppm LEV, 5 ppm LAN, and 10 ppm TC were prepared in both Milli-Q (MQ) water and pre-filtered tap water (TAP) to examine the influence of the water matrix on catalytic performance. To evaluate the impact of representative ions on photocatalytic mineralization, a multipollutant solution (5 ppm LEV, 5 ppm LAN, 10 ppm TC) in Milli-Q water was spiked with NaCl, $NaHCO_3$, $NaNO_3$, Na_2SO_4, Na_3PO_4, KNO_3, $Ca(NO_3)_2$, $Mg(NO_3)_2$, $Fe(NO_3)_3$, and $Cu(NO_3)_2$ at concentrations of 1, 5, and 10 mM. Mineralization efficiency was measured after 30 min of UV-A or visible light irradiation in the presence of 2.5 mM PMS using 5 nm SnO_2-BiOI and 5 nm TiO_2-BiOI photocatalysts. TOC removal was used to calculate relative mineralization compared to control samples without added salts.

Catalyst stability was evaluated through a reusability study in multipollutant solutions. Each sample underwent 10 consecutive 90-minute cycles, with TOC measurements performed at the end of each cycle to monitor mineralization efficiency.

2.4. Hydroxyl and sulfate radical generation of (Pd)-SnO_2-BiOI and (Pd)-TiO_2-BiOI thin films

The concentrations of sulfate and hydroxyl radicals were determined using spectrophotometric and fluorometric methods. Sulfate radical concentrations were quantified via UV–visible spectrophotometry by detecting the formation of Ce(IV) at 320 nm, based on the oxidation of Ce(III). Hydroxyl radical concentrations were measured using sodium terephthalate (Na_2TPA) as a fluorogenic probe, tracking the formation of sodium hydroxyterephthalate (hTPA) through fluorescence spectroscopy. A 1 mM Na_2TPA solution was prepared in a pH 7.4 buffer and mixed with PMS. Fluorescence intensity was recorded using an AMINCO-Bowman Series 2 spectrofluorometer, with excitation at 315 nm and emission at 425 nm, as hTPA exhibits strong fluorescence in this range. Time-dependent fluorescence measurements were performed to monitor hydroxyl radical formation under various heating conditions, both with and without a catalyst. A calibration curve correlating fluorescence intensity to known hTPA concentrations enabled hydroxyl radical quantification [60].

2.5. Photostability of (Pd)-SnO_2-BiOI and (Pd)-TiO_2-BiOI thin films

The photostability of thin films was assessed under visible and UV light irradiation for 360 min in the presence and absence of PMS and/or organic pollutant (180 ppm of TC). The integrity of the catalyst was evaluated by quantifying bismuth, titanium, and/or tin ion concentrations. Measurements were conducted using inductively coupled plasma optical emission spectroscopy (ICP-OES, Optima 8300, PerkinElmer) for concentrations in the ppm range, and inductively coupled plasma mass spectrometry (ICP-MS, NexION 2000, PerkinElmer) for trace-level detection in the ppb range. The presence of iodine species was determined via anion-exchange chromatography with postcolumn reaction and UV/visible detection. A Dionex DX-500 ion chromatography system was employed, equipped with a Dionex PC 10 reagent delivery module, an ASRS-I membrane-exchange suppressor, and a Spectroflow 773 absorbance detector. Iodide separation was conducted using a Dionex AG 11/AS 11 column with a 60 mM of sodium bromide (NaBr, Sigma-Aldrich, CAS: 7647-15-6), 1 mM of sodium hydroxide (NaOH, Sigma-Aldrich, CAS: 1310-73-2) eluent. Postcolumn reaction with 5 μM of bromine (Br_2, Sigma-Aldrich, CAS: 7726-95-6) in 2 mM NaOH converted iodide to IBr_2^-, which was detected at 249.5 nm. All reagents were of the highest purity, and standard solutions were freshly prepared in Milli-Q water.

3. Results and discussion

The ALD-engineered (Pd)-SnO_2- and (Pd)-TiO_2-BiOI thin films were rationally designed to (i) mitigate photocorrosion of BiOI and (ii) enhance hydroxyl radical production under visible light irradiation, thereby improving photocatalytic performance. ALD was selected due to its precise, atomic-level control over nanometric thin-film deposition, ensuring uniformity, conformality, and monolayer growth per cycle. This makes ALD an ideal technique for depositing ultra-thin layers of TiO_2 or SnO_2 and Pd nanoparticles on BiOI. The material selection for these heterojunctions was based on key optoelectronic and photocatalytic properties, including electron mobility, charge separation, light absorption, bandgap of metal oxides, and electron transport efficiency, all of which contribute to enhanced degradation of organic pollutants via PMS activation.

In the BiOI/TiO_2 heterojunction, a type-II band alignment is formed due to their distinct energy band positions (Scheme 1). BiOI, with its narrow bandgap (~1.8–2.0 eV), has a conduction band minimum (CBM) at approximately −4 eV and a valence band maximum (VBM) at approximately −5.8 eV, enabling visible-light absorption. Valence band value of BiOI is too low to form •OH, because oxidation potential of h^+ is lower than redox potential $^{\bullet}OH/OH^-$ ($E^0 = 2.38$ V) (59, 60) [37,61–63]. In contrast, TiO_2, a wide-bandgap semiconductor (~3.2 eV), has its CBM at approximately −4.2 eV and VBM at approximately −7.4 eV, making it UV-active and an effective electron transport layer. The staggered band alignment facilitates charge separation, as photogenerated electrons migrate from the CB of BiOI to TiO_2, while holes migrate from TiO_2 to BiOI, reducing recombination losses. This charge redistribution prevents electron accumulation in BiOI, thereby enhancing charge lifetime, while also preventing hole accumulation in TiO_2, which could otherwise lead to recombination losses. The spatial separation of charge carriers at different material interfaces further reduces recombination, extending charge carrier lifetimes and improving optoelectronic and photocatalytic performance [62,64–68].

Similarly, in the BiOI/SnO_2 heterojunction, a type-II band alignment is also formed due to their distinct energy band positions, facilitating efficient charge separation and transfer (Scheme 1). BiOI has a CBM at approximately −4 eV and VBM at approximately −5.8 eV, allowing visible-light absorption, while SnO_2, with a wider bandgap (~3.3–3.6 eV), has its CBM at −4.5 eV and VBM at −8.0 eV, primarily absorbing UV light. A key advantage of SnO_2 is its significantly higher electron mobility (~100–200 $cm^2\ V^{-1}s^{-1}$) compared to TiO_2 (~0.1–10 $cm^2\ V^{-1}s^{-1}$), which enhances charge transport efficiency [62,64–66,69]. The staggered band alignment allows electrons to transfer from BiOI to SnO_2, while holes migrate from SnO_2 to BiOI, further improving charge separation and minimizing recombination. Upon illumination, BiOI generates electron-hole pairs, which, in the absence of SnO_2, would rapidly recombine, reducing efficiency. However, the BiOI/SnO_2 heterojunction prevents electron accumulation, thereby improving charge carrier lifetime, oxidation efficiency, and overall photocatalytic activity [62,64–66,68]. The proposed band edge positions and charge transfer directions were deduced based on literature-reported conduction and valence band values for BiOI, SnO_2, and TiO_2, combined with our PL quenching results (see section 3.1 and 3.2), which are consistent with efficient charge separation expected for type-II heterojunctions.

The BiOI/SnO_2 heterojunction exhibits superior performance over BiOI/TiO_2, primarily due to the higher electron mobility of SnO_2, which results in faster charge transfer and lower recombination rates. While both heterojunctions benefit from visible-light absorption (BiOI) and UV activity (metal oxide), SnO_2 serves as a more effective electron transport layer, enhancing conductivity. Although TiO_2 has a slightly lower bandgap, this difference is negligible compared to the superior charge transport and photocatalytic efficiency of BiOI/SnO_2.

While TiO_2 and SnO_2 improve charge separation and reduce recombination losses, they do not fully eliminate photocorrosion risks. The incorporation of SnO_2 and TiO_2 on BiOI is thus justified not only by

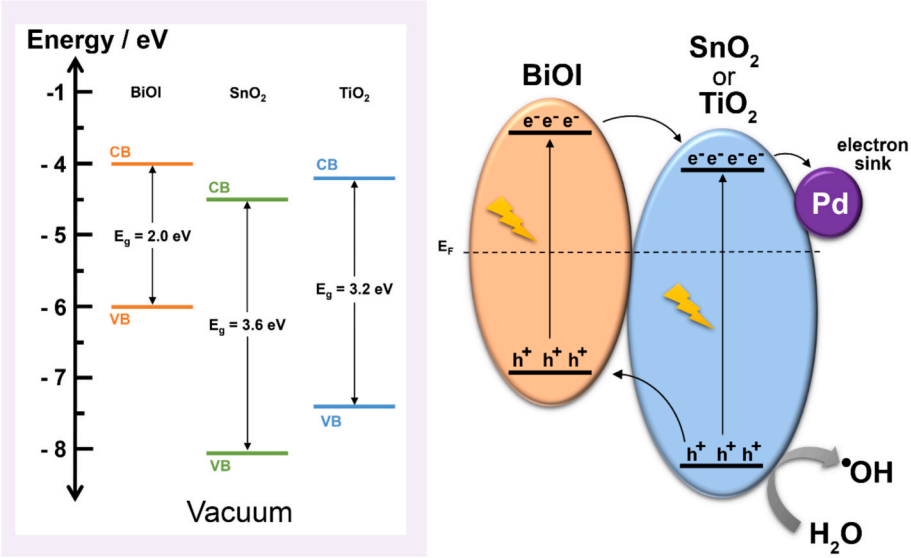

Scheme 1. Band edge positions in vacuum for BiOI, SnO_2, and TiO_2, along with a schematic representation of Pd-SnO_2 and Pd-TiO_2-BiOI Type II heterojunctions, incorporating a palladium Schottky junction.

their type-II band alignment but also by their established roles in facilitating PMS activation, as demonstrated in prior PMS-driven AOP systems. These oxides create efficient pathways for electron transfer, which reduces recombination losses and enhances the generation of $SO_4^{\bullet-}$ radicals, making them ideal candidates for heterostructure engineering in sulfate-radical-based water purification technologies. The addition of a Pd nanoparticles onto BiOI/TiO_2 or BiOI/SnO_2 further enhances stability by acting as an electron sink, catalyzing oxygen reduction reactions, and redirecting photogenerated electrons away from BiOI, thereby reducing recombination and slowing self-oxidation. The formation of a Schottky junction at the Pd-metal oxide interface prevents electron backflow and facilitates rapid electron transfer, increasing charge carrier lifetime. Furthermore, localized surface plasmon resonance in Pd nanoparticles enhances charge separation, while Pd's catalytic activity inhibits iodide oxidation, preventing BiOI degradation. However, Pd modification may suppress hydroxyl radical formation, which could affect pollutant mineralization efficiency. This occurs because Pd catalyzes direct oxygen reduction, reducing the formation of superoxide and subsequent hydroxyl radicals.

To address these challenges, five different BiOI-based heterojunction materials were systematically investigated, focusing on photocorrosion activity, hydroxyl radical generation, and visible-light-driven PMS-activated mineralization of organic pollutants. The results provide critical insights into the role of Pd, SnO_2, and TiO_2 in enhancing photostability, charge transport, and catalytic efficiency, ultimately guiding the rational design of advanced visible light-driven PMS-activated mineralization of organic pollutants.

3.1. Synthesis and characterization of (Pd)-SnO_2-BiOI and (Pd)-TiO_2-BiOI thin films

The synthesis of BiOI thin films was carried out via electrodeposition on 0.8 cm^2 FTO glass, resulting in a uniform orange colored film. A total charge of 0.35 C was applied to achieve a film thickness of approximately 1 μm. The electrodeposited BiOI films morphology was examined using FE-SEM, revealing vertically oriented nanoplates with consistent thicknesses and shape, randomly arranged in various directions, often intersecting each other (Fig. S1).

Following the BiOI electrodeposition, nanometric layers (1 nm, 5 nm and, 10 nm) of SnO_2 or TiO_2 were conformally deposited on BiOI via ALD. Immediately after deposition, the samples appeared black due to the elevated temperature of the ALD process but reverted to their native orange color upon cooling to room temperature. Subsequently, an additional Pd nanoparticle layer was deposited on SnO_2-BiOI and TiO_2-BiOI samples via ALD. Unlike the SnO_2 and TiO_2 coatings, Pd-modified samples retained their black coloration even after cooling, indicating potential changes in optical or electronic properties.

The morphology of the samples was further analyzed using FE-SEM (Fig. 1). Morphology analysis did not show relevant differences between 1 nm, 5 nm and 10 nm thickness of SnO_2 and TiO_2 films. The 5 nm SnO_2-BiOI (Fig. 1a) and 5 nm TiO_2-BiOI (Fig. 1b) samples did not exhibit significant morphological changes compared to pristine BiOI (Fig. S1a). The characteristic nanoplate structure of BiOI was preserved, confirming that the ALD deposition process did not alter BiOI morphology while ensuring the homogeneous deposition of SnO_2 and TiO_2. However, after Pd deposition (Fig. 1c, 1d), small spherical agglomerates were observed on the nanoplates, particularly in the Pd-SnO_2-BiOI samples. These features likely result from Pd mobility during the nucleation phase, leading to localized aggregation on the BiOI surface. Elemental distribution was further assessed via EDS mapping (Fig. S1b–g), which revealed uniform deposition of Sn and Ti across the BiOI film surface. Although Pd was not resolved in the elemental maps due to its low content and the nanoscale dimensions of the deposited particles, its presence was confirmed by XPS analysis.

To further verify that the ALD-grown SnO_2 and TiO_2 layers do not block incident light from reaching the BiOI layer, optical power transmission measurements were carried out under the same UV-A and visible-light conditions used during photocatalytic experiments. Substrates containing 5 nm of SnO_2 or TiO_2, with and without Pd (1 nm equivalent thickness), were tested. The measurements show that the oxide layers alone transmit over 93 % of visible light and ~87 % of UV-A. When coated with Pd, a slight reduction in transmission (~3–5 %) was observed, yet the overall light penetration remained high (above 80–85 % in UV-A). These data confirm that the ALD layers do not significantly limit photon flux to the BiOI nanosheets and support the validity of the heterojunction model presented in Scheme 1.

Fig. 2 shows the characterization of the surface chemical nature using XPS. Bi 4f, I 3d, and O 1s spectra were analyzed in all samples to evaluate if BiOI film was modify after ALD. The binding energies obtained from the XPS analysis were calibrated for specimen charging by referencing the C 1s peak at 284.6 eV. The Bi 4f, I 3d, and O 1s spectra were analyzed for all samples. SnO_2 and TiO_2 thickness variation did not show significant differences in XPS analysis. Fig. 2 shows 5 nm SnO_2 −BiOI and 5 nm TiO_2-BiOI synthetized samples. The Bi 4f peaks at 159.3

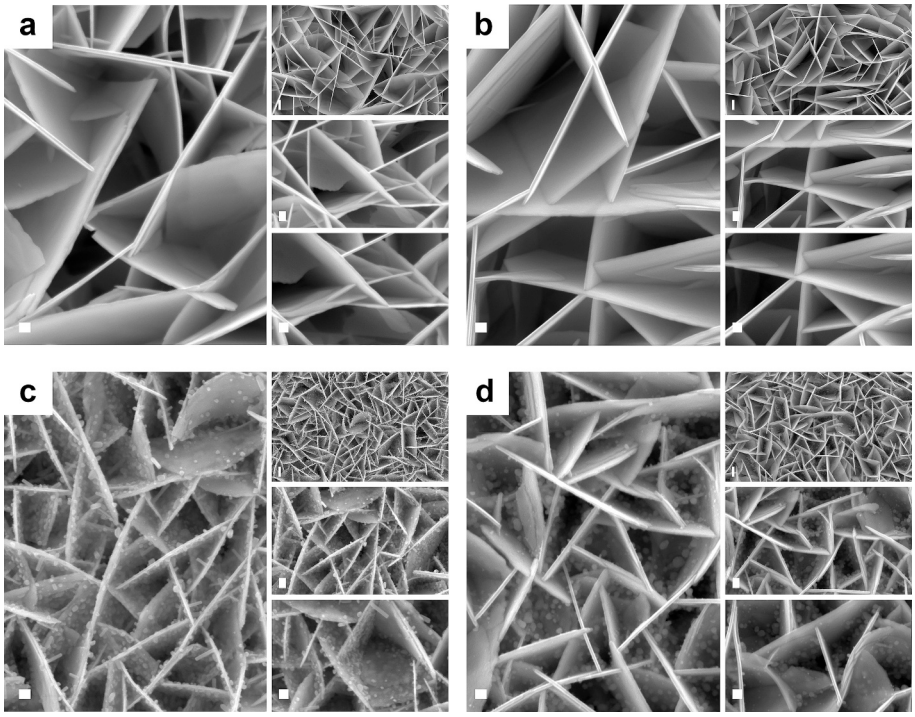

Fig. 1. FE-SEM micrograph of (a) SnO_2-BiOI, (b) TiO_2-BiOI, (c) Pd-SnO_2-BiOI, and (d) Pd-TiO_2-BiOI thin films. Scale bar: 100 nm.

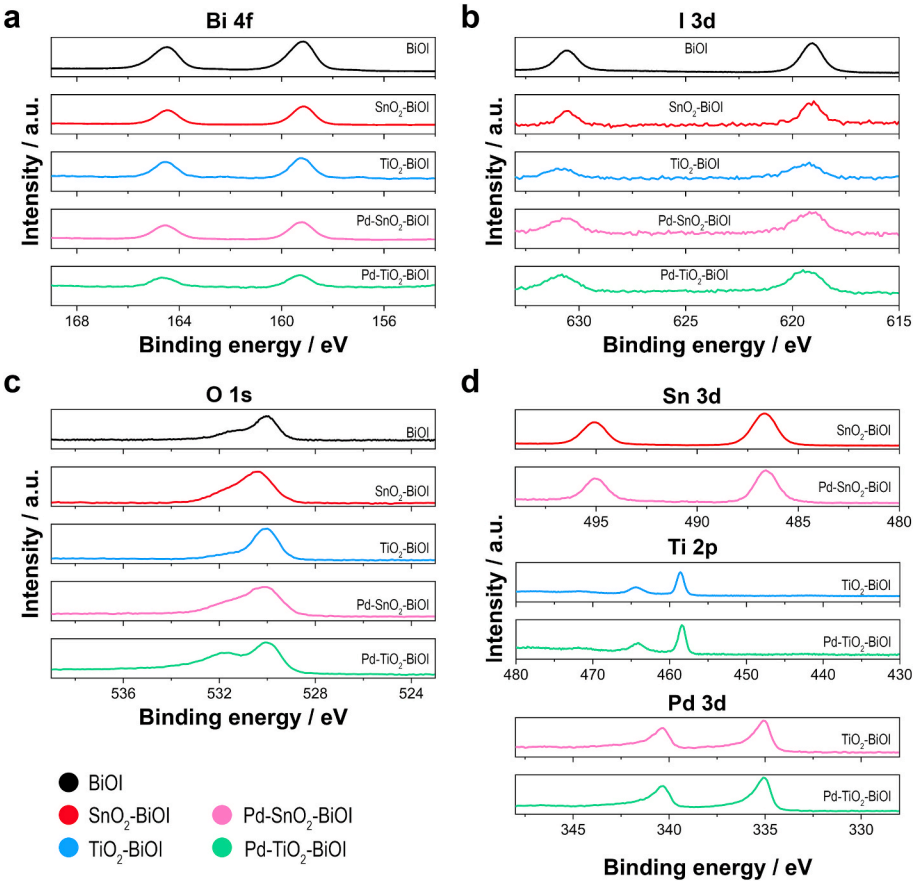

Fig. 2. X-ray photoelectron spectroscopy (XPS) spectra for (a) Bi 4f, (b) I 3d, (c) O 1s, and (d) Sn 3d, Ti 2p and Pd 3d spectra of 5 nm SnO_2 −BiOI or 5 nm TiO_2-BiOI synthetized samples.

eV and 164.6 eV, corresponding to Bi^{3+} $4f_{7/2}$ and Bi^{3+} $4f_{5/2}$, respectively, confirm the presence of $[Bi_2O_2]^{2+}$ Bi-O bonds. Similarly, the I 3d peaks at 619.2 eV and 630.6 eV, corresponding to I $3d_{5/2}$ and I $3d_{3/2}$, were observed in all samples. The alignment of Bi 4f and I 3d peaks across all samples indicates that the BiOI films retain their original oxidation states, confirming that ALD deposition did not alter the BiOI chemical composition [27,31].

Differences among the samples were primarily observed in the O 1s spectra, where an asymmetric peak at 529.7 eV confirmed the presence of Bi-O bonds in all samples. A shoulder peak at 531.3 eV, associated with hydroxyl groups from adsorbed water, varied slightly among samples, likely due to differences in surface humidity. The Sn 3d spectrum of the SnO_2-BiOI sample exhibited peaks at 486.5 eV and 495.0 eV, corresponding to Sn $3d_{5/2}$ and Sn $3d_{3/2}$, confirming the presence of Sn^{4+} species [38,70]. Similarly, the Ti 2p spectrum of the TiO_2-BiOI sample exhibited peaks at 458.7 eV and 464.1 eV, corresponding to Ti $2p_{3/2}$ and Ti $2p_{1/2}$, indicating the presence of Ti^{4+} species [71,72]. Additionally, Pd deposition was confirmed in Pd-SnO_2-BiOI and Pd-TiO_2-BiOI samples, as shown in Fig. 2**d**. The Pd 3d spectrum exhibited peaks at 335.4 eV and 340.5 eV, corresponding to Pd $3d_{5/2}$ and Pd $3d_{3/2}$, confirming the presence of Pd^0 species. The asymmetry of these peaks suggests interactions between Pd and other surface species [73].

Furthermore, XRD analysis (**Fig. S2a**) confirmed the formation of tetragonal-phase BiOI, based on the characteristic reflection peaks at approximately $2\theta = 29.8°$, 31.7°, 45.4°, and 55.3°, which match the JCPDS card No. 73–2062. Additional peaks observed at $2\theta = 26.6°$, 34.0°, 37.8°, 46.6°, 51.6°, 56.7°, and 61.8° correspond to the FTO substrate. However, in SnO_2-BiOI and TiO_2-BiOI samples, no distinct diffraction peaks corresponding to SnO_2 or TiO_2 were detected, suggesting that the ultrathin SnO_2 and TiO_2 layers deposited via ALD were below the XRD detection limit. Additionally, the possibility that these oxide layers were partially or fully amorphous cannot be excluded, as ALD-grown films at low temperatures often exhibit limited crystallinity. These results indicate that the deposition did not introduce significant structural differences between the samples [27,31].

To gain further insights into the charge separation efficiency of the synthesized photocatalysts, steady-state PL spectra were recorded under 365 nm excitation (**Fig. S2b**). All tested samples exhibited a broad emission band between 525 and 700 nm, attributed to radiative recombination of photoinduced electron–hole pairs in BiOI-based structures. Pristine BiOI showed the highest PL intensity, indicating rapid recombination. In contrast, both 5 nm SnO_2–BiOI and 5 nm TiO_2–BiOI heterojunctions exhibited significantly quenched PL signals, confirming that the formation of type-II heterostructures effectively suppresses recombination by promoting directional charge transfer across the heterojunction interface. Even more strikingly, Pd-decorated heterostructures (Pd–TiO_2–BiOI and Pd–SnO_2–BiOI) demonstrated the lowest PL intensities among all tested samples. This attenuation reflects the role of Pd nanoparticles as electron sinks due to the formation of Schottky junctions at the metal–semiconductor interface, further enhancing charge separation and prolonging charge carrier lifetime. These findings validate the synergistic function of type-II heterojunctions and Schottky barriers in suppressing charge recombination and improving photocatalytic performance, as previously hypothesized.

3.2. PMS catalytic degradation and mineralization of organic pollutants

To evaluate the contribution of surface adsorption prior to PMS activation, adsorption–desorption equilibrium tests were conducted under dark conditions for all catalyst systems. TC adsorption was measured after 30 min of equilibration in the absence of light and PMS. The results showed moderate adsorption percentages: 17 %, 13 %, and 9 % for 1, 5, and 10 nm SnO_2-BiOI films, respectively, and 14 %, 11 %, and 8 % for the corresponding TiO_2-BiOI films. Notably, Pd-functionalized heterojunctions exhibited the highest adsorption levels, with 23–24 % for Pd–SnO_2–BiOI and 19–21 % for Pd–TiO_2–BiOI. These values confirm that although surface adsorption contributed to initial pollutant uptake, the dominant removal mechanism arose from PMS activation under illumination, as evidenced by the sharp increase in degradation rates upon PMS addition.

In parallel, the effect of pH and catalyst surface charge was evaluated based on the point of zero charge (pH_{zpc}) of the heterostructures. Literature values indicate that TiO_2 and SnO_2 possess pH_{zpc} values between 5.5 and 6.5 and 4.0–5.0, respectively, with Pd decoration slightly lowering these thresholds due to increased surface acidity. At the experimental pH (~7.0), TiO_2- and SnO_2-based films exhibit a slightly negative surface charge, while tetracycline predominantly exists in a zwitterionic form. Although this does not result in strong electrostatic attraction, the lack of repulsion – combined with the presence of both positively and negatively charged sites on TC – supports sufficient interaction between the catalyst surface and the antibiotic. This proximity facilitates radical-mediated degradation once PMS is activated under illumination.

Therefore, the photocatalytic degradation of TC was investigated using a 20 ppm solution at pH 7 over a 90-minute period under various conditions: visible or UV light irradiation, the presence of PMS (2.5 mM), and their combinations. Prior to the degradation and mineralization experiments, the stability of the TC solution was assessed in the absence of light and PMS, confirming no significant TOC variations over 60 days. Different thicknesses (1 nm, 5 nm and 10 nm) of SnO_2 and TiO_2 layers were deposited via ALD on electrodeposited BiOI film, so this study also aims to determine the optimal thickness of the deposits to maximize the efficiency of the base-material for the degradation and mineralization of pollutants. Once optimal thickness for photocatalysis was determined, Pd nanoparticles added via ALD was evaluated in terms of photocatalysis efficiency.

BiOI exhibited moderate photocatalytic activity, serving as the benchmark for comparison with heterojunction systems (Fig. S3). Under visible light, BiOI achieved 22.4 ± 0.9 % degradation and 12.45 ± 1.2 % mineralization, indicating limited electron-hole separation and low mineralization efficiency. The presence of PMS improved performance, increasing degradation to 48.4 ± 1.3 % and mineralization to 36.0 ± 0.6 %, demonstrating PMS activation in BiOI-driven photocatalysis. Under UV light, degradation reached 66.7 ± 1.0 %, with 48.0 ± 0.7 % mineralization, highlighting the improved efficiency under higher-energy irradiation. The best performance was recorded under UV + PMS conditions, where degradation reached 83.1 ± 0.9 % and mineralization 75.0 ± 1.2 %, suggesting enhanced oxidative degradation due to the synergistic effect of UV irradiation and PMS activation. However, despite these improvements, BiOI's photocatalytic efficiency remained lower than that of SnO_2-BiOI and TiO_2-BiOI heterojunctions, indicating that additional modifications are required to enhance its charge separation and stability.

Fig. S4 illustrates the degradation of TC over 90 min for samples with different film thicknesses under various conditions. The results for SnO_2-BiOI (Fig. S4a and 3a) indicate that under UV + PMS conditions, all SnO_2 thicknesses exhibit similar degradation performance (~86 %). However, in other cases, a 5 nm SnO_2 film outperforms a 1 nm film. The degradation efficiency increases from 37.6 ± 0.7 % (1 nm SnO_2) to 61.4 ± 0.1 % (5 nm SnO_2) under visible light, from 53.8 ± 0.5 % to 63.4 ± 1.1 % under visible + PMS, from 68.6 ± 0.4 % to 77.1 ± 1.5 % under UV light, and from 52.9 ± 1.3 % to 57.1 ± 1.2 % in PMS (absence of light).

However, increasing the SnO_2 thickness to 10 nm results in reduced degradation efficiency: 50.2 ± 0.5 % under visible light, 58.8 ± 1.3 % under visible + PMS, 71.9 ± 1.2 % under UV light, and 43.4 ± 0.9 % in PMS (dark conditions). These results confirm that a nanometric SnO_2 layer enhances the contaminant degradation efficiency of BiOI, but beyond a certain thickness, efficiency decreases possibly because excessive SnO_2 coverage inhibits the synergistic effect with BiOI. The optimal thickness for TC degradation is determined to be 5 nm. These findings confirm that the photocatalytic properties of SnO_2-BiOI effectively promote PMS activation, particularly under UV light, achieving

high TC degradation.

For the TiO_2-BiOI samples, a 5 nm TiO_2 deposit significantly enhances degradation performance compared to a 1 nm film (Fig. S4b and 3b). The degradation efficiency increases from 50.9 ± 1.7 % to 62.3 ± 2.9 % under visible irradiation, from 80.7 ± 0.2 % to 89.8 ± 2.9 % under visible light + PMS, from 82.2 ± 1.1 % to 92.7 ± 0.2 % under UV irradiation, and from 87.7 ± 2.2 % to 95.2 ± 2.1 % under UV + PMS conditions. Additionally, when the TiO_2 thickness is increased to 10 nm, degradation performance decreases to 56.6 ± 2.1 % (visible irradiation), 80.1 ± 1.1 % (visible + PMS), 77.8 ± 1.1 % (UV irradiation), and 85.6 ± 1.2 % (UV + PMS). Under PMS in dark conditions, degradation remains similar across all thicknesses (~66 %). These results confirm that the optimal TiO_2 thickness for TC degradation is 5 nm. The 5 nm TiO_2-BiOI samples demonstrate excellent degradation performance under UV irradiation, highlighting the high photocatalytic properties of the material. Furthermore, the high efficiency observed under visible light + PMS (89.8 ± 2.9 %) confirms that 5 nm TiO_2-BiOI is an optimal candidate for real-world water treatment applications.

To further evaluate catalytic efficiency, an additional Pd nanoparticle layer was deposited on the 5 nm SnO_2-BiOI and 5 nm TiO_2-BiOI samples, as they exhibited the best performance (Fig. S4c and 3c). For Pd-SnO_2-BiOI, degradation under UV irradiation is significantly reduced

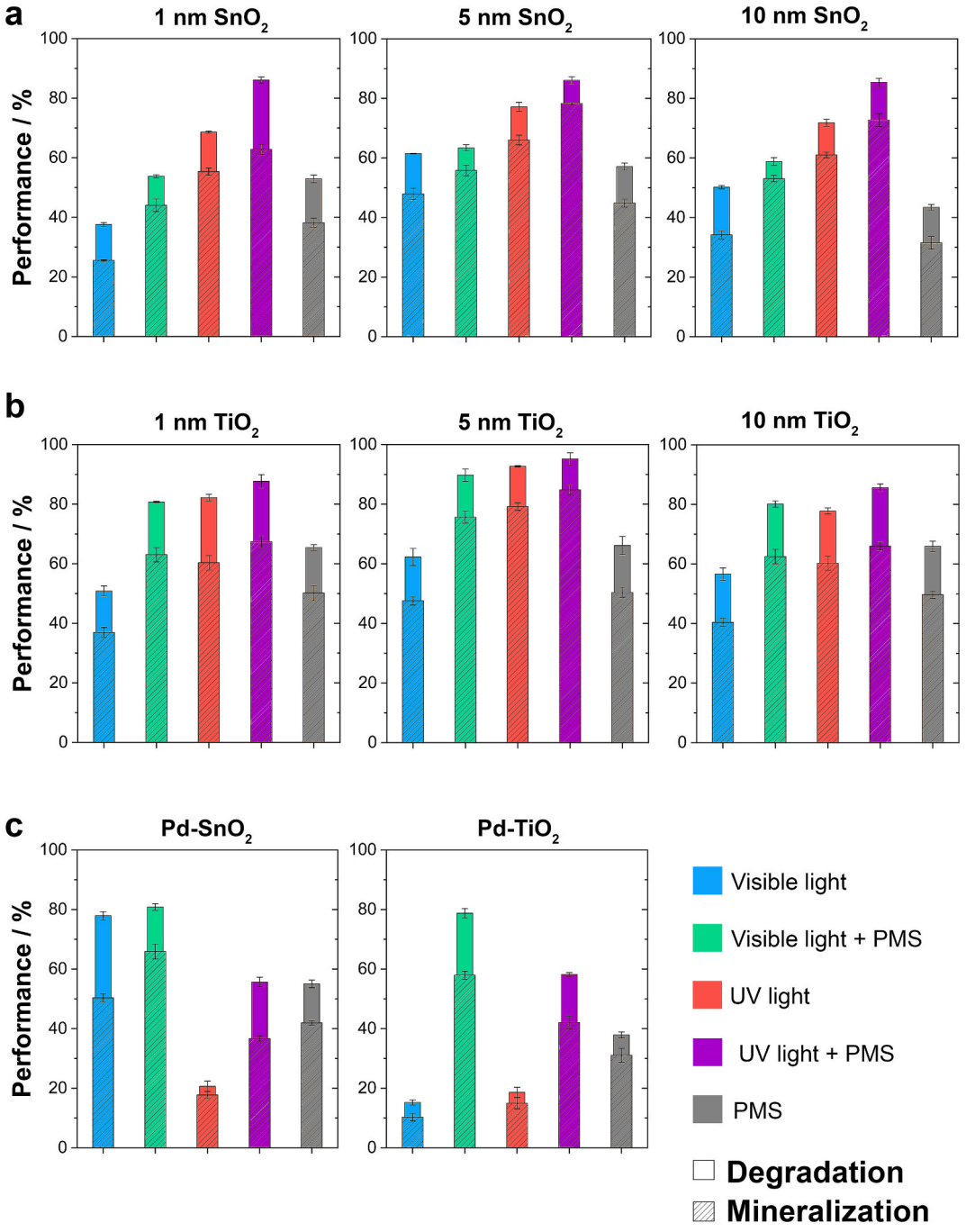

Fig. 3. TC degradation and mineralization performance as a function of SnO_2 and TiO_2 thickness in different catalytic systems after 90 min of treatment. (a) Performance of SnO_2-BiOI and (b) TiO_2-BiOI with oxide thicknesses of 1 nm (left), 5 nm (center), and 10 nm (right). (c) Comparison of degradation and mineralization efficiency for Pd-SnO_2-BiOI and Pd-TiO_2-BiOI under different conditions. In Pd-based materials, the SnO_2 and TiO_2 thickness is fixed at 5 nm. Experimental conditions: $[TC]_0$ = 20 ppm, $[PMS]_0$ = 0 or 2.5 mM, T = 25 °C. All experiments were conducted in triplicate, and error bars represent standard deviations.

to 20.7 ± 1.7 %. Under PMS in darkness and UV irradiation, similar degradation levels are observed, reaching 55.1 ± 1.3 % and 55.7 ± 1.6 %, respectively, indicating that the Pd deposit negatively impacts the catalytic capacity in these conditions. However, under visible light, both with and without PMS, Pd-SnO_2-BiOI outperforms the non-Pd samples, achieving 80.8 ± 1.1 % and 77.9 ± 1.3 % degradation, respectively. In contrast, Pd-TiO_2-BiOI samples exhibit lower degradation efficiencies than their non-Pd counterparts: 15.2 ± 0.9 % under visible light, 18.6 ± 1.7 % under UV light, 37.9 ± 1.0 % under PMS in darkness, 58.2 ± 0.7 % under UV + PMS, and 78.8 ± 1.6 % under visible light + PMS. These results indicate that Pd deposition on TiO_2-BiOI is not beneficial for water treatment, as it reduces TC degradation efficiency.

Mineralization efficiency, assessed via TOC analysis, was lower than degradation efficiency across all samples, indicating that while TC degraded into smaller compounds, complete mineralization to CO_2 and H_2O was not achieved within 90 min.

For SnO_2-BiOI samples (Fig. 3a), a 5 nm SnO_2 layer significantly outperformed a 1 nm layer, achieving higher mineralization under all conditions: 44.9 ± 1.4 % vs. 25.5 ± 0.3 % (PMS, dark), 47.9 ± 1.9 % vs. 38.2 ± 1.5 % (visible), 55.8 ± 1.8 % vs. 44.1 ± 2.1 % (visible + PMS), 66.0 ± 1.6 % vs. 55.4 ± 1.3 % (UV), and 78.3 ± 0.3 % vs. 62.8 ± 1.7 % (UV + PMS). Increasing SnO_2 thickness to 10 nm reduced mineralization in all cases. Fig. 3 also verifies that UV + PMS provides the most efficient mineralization pathway.

For TiO_2-BiOI (Fig. 3**b**), the 5 nm TiO_2 sample exhibited the highest mineralization performance: 47.6 ± 1.4 % (visible), 50.4 ± 1.7 % (PMS, dark), 75.7 ± 2.0 % (visible + PMS), 79.2 ± 1.3 % (UV), and 84.8 ± 1.5 % (UV + PMS), outperforming 1 nm and 10 nm deposits. These results confirm 5 nm TiO_2-BiOI as an optimal candidate for water decontamination, particularly under visible and UV light for PMS activation.

Since 5 nm SnO_2-BiOI and 5 nm TiO_2-BiOI exhibited the best performance, their mineralization was further evaluated after Pd deposition via ALD (Fig. 3c). The highest mineralization occurred under visible + PMS conditions, reaching 65.9 ± 2.5 % (Pd-SnO_2-BiOI) and 58.0 ± 1.4 % (Pd-TiO_2-BiOI). However, under visible light (without PMS), Pd-SnO_2-BiOI maintained higher mineralization (50.3 ± 1.4 %), whereas Pd-TiO_2-BiOI dropped significantly (10.3 ± 1.3 %). PMS in darkness yielded similar results for both (41.9 ± 0.7 % vs. 31.1 ± 2.4 %). Under UV conditions, Pd deposition negatively impacted performance, with Pd-SnO_2-BiOI achieving only 36.7 ± 0.9 % (UV + PMS) and 17.7 ± 1.2 % (UV), while Pd-TiO_2-BiOI reached 42.0 ± 2.1 % (UV + PMS) and 15.0 ± 1.9 % (UV). Therefore, Pd deposition only enhanced mineralization for Pd-SnO_2-BiOI under visible light (with and without PMS), while it negatively affected Pd-TiO_2-BiOI performance across all conditions. This contrasting behavior can be attributed to differences in band alignment, charge transfer dynamics, and the interaction of Pd with the underlying oxide. In the SnO_2-BiOI system, BiOI is primarily responsible for light absorption, and Pd acts as an efficient electron trap via Schottky junction formation, promoting charge separation and enhancing PMS activation. Under UV-A, SnO_2 does not strongly compete with BiOI for excitation, allowing the beneficial role of Pd to persist. In contrast, TiO_2 absorbs UV-A efficiently, and photogenerated electrons in TiO_2 may preferentially transfer to Pd rather than migrate across the TiO_2-BiOI interface. This alternative pathway may suppress the formation of a Type-II charge separation and diminish photocatalytic efficiency. Furthermore, the higher conduction band level of TiO_2 compared to SnO_2 enhances electron transfer to Pd, which can alter the charge separation dynamics. In TiO_2-based heterostructures, this may suppress interfacial charge transfer to BiOI and reduce ROS generation via PMS activation, especially if electrons accumulate excessively on Pd or bypass key reaction pathways. These findings highlight that while Pd effectively enhances visible-light-driven activity in both systems, its influence under UV-A is dictated by the photoactive component, band alignment, and competitive electron pathways. This underscores the need to adapt cocatalyst strategies to the specific semiconductor pairing and irradiation regime.

Importantly, the effects of PMS concentration and solution pH on mineralization efficiency were systematically investigated under both UV-A and visible light conditions, revealing that optimal degradation occurs at 5–7.5 mM PMS and pH 6.0–7.0, as detailed in Tables S1 and S2.

To elucidate the photocatalytic mechanism of 5 nm SnO_2-BiOI and 5 nm TiO_2-BiOI heterostructures in PMS-assisted degradation of TC, radical trapping experiments were performed using specific scavengers (Fig. S5). The impact on degradation efficiency allowed the identification of the dominant reactive species. Without scavengers, degradation efficiencies reached 86.1 ± 1.2 % (UV + PMS) and 63.4 ± 1.1 % (visible + PMS) for SnO_2-BiOI, and 95.2 ± 2.1 % (UV + PMS) and 89.8 ± 2.9 % (visible + PMS) for TiO_2-BiOI. The addition of BQ, a superoxide radical ($O_2^{\bullet-}$) quencher, caused moderate declines: 71.5 ± 1.3 % (UV) and 53.3 ± 1.8 % (visible) for SnO_2-BiOI, and 81.9 ± 1.8 % (UV) and 74.4 ± 1.4 % (visible) for TiO_2-BiOI. This suggests a contributory, though secondary, role of $O_2^{\bullet-}$. Methanol, a quencher of both hydroxyl ($^{\bullet}OH$) and sulfate ($SO_4^{\bullet-}$) radicals, caused a drastic drop in efficiency – below 11 % (UV) and 17 % (visible) for both heterostructures – highlighting the central role of these species, especially under UV irradiation. TBA, selective for $^{\bullet}OH$, also significantly reduced activity: 43.2 ± 2.3 % (UV) and 38.4 ± 1.0 % (visible) for SnO_2-BiOI, and 48.6 ± 1.3 % (UV) and 53.9 ± 2.4 % (visible) for TiO_2-BiOI. This points to $^{\bullet}OH$ radicals as major contributors, though the more severe inhibition by MeOH implies $SO_4^{\bullet-}$ plays a more pivotal role in early degradation steps. EDTA, a hole (h^+) scavenger, reduced degradation by less than 6 % across all conditions, indicating a minor role of h^+ in the process. In summary, hydroxyl and sulfate radicals are the dominant reactive species in the photocatalytic PMS activation mechanism of TC degradation by SnO_2-BiOI and TiO_2-BiOI heterostructures. These insights provide a foundation for optimizing photocatalyst design to enhance ROS generation and improve degradation efficiency.

In addition, the photocatalytic degradation of TC by 5 nm SnO_2-BiOI and 5 nm TiO_2-BiOI samples was investigated through HPLC-MS analysis to identify intermediate products (Fig. S6). Plausible degradation pathways were proposed for the SnO_2-BiOI + PMS and TiO_2-BiOI + PMS systems based on the detected species (Fig. S7). TC molecules contain electron-rich functional groups, including double bonds, phenol moieties, and amino groups, which exhibit heightened susceptibility to attack by ROS. The degradation process can be broadly divided into four stages: hydroxylation, demethylation, ring opening, and eventual mineralization into small organic fragments. Comparable results were obtained for 5 nm SnO_2-BiOI and 5 nm TiO_2-BiOI under both UV-A and visible-light irradiation conditions employed during the photocatalytic experiments.

The parent compound, TC, has an initial mass-to-charge ratio (m/z) of 445. In the initial phase of degradation, hydroxylation results in the formation of P1 (m/z = 459) and P4 (m/z = 477). In Pathway I, the continuation of the ROS attack causes P1 to undergo water molecule desorption, deamidation, and demethylation, successively forming P4 (m/z = 459), P2 (m/z = 400), and P3 (m/z = 343). In Pathway II, P4 undergoes a series of chemical reactions, including demethylation and amino group cleavage, resulting in the formation of P5 (m/z = 340). This is followed by further processing through dehydroxylation, methylation, additional amine cleavage, and ring opening, culminating in the production of P6 (m/z = 230). In Pathway III, a sequential loss of methyl, amino, carbonyl, and hydroxyl groups, accompanied by ring cleavage, results in the generation of intermediates P7 (m/z = 417), P8 (m/z = 362), and P9 (m/z = 227). These intermediate species then undergo further oxidative fragmentation, including aromatic ring cleavage and removal of residual functional groups, yielding smaller molecules such as P10 (m/z = 90), P11 (m/z = 85), and P12 (m/z = 73). These low-molecular-weight compounds signify advanced stages of degradation, which ultimately result in complete mineralization into CO_2, H_2O, and inorganic ions.

Given the superior performance of 5 nm SnO_2-BiOI and 5 nm TiO_2-BiOI, their photocatalytic versatility was assessed through TOC analysis in different contaminant solutions: 20 ppm levofloxacin (LEV), 5 ppm

lansoprazole (LAN), and a multipollutant solution (MP) containing 5 ppm LEV, 5 ppm LAN, and 10 ppm TC. To evaluate real-world applicability, experiments were also conducted in tap water (collected from the University of Barcelona, pH 7.75, total hardness 234 mg $CaCO_3$ L^{-1}, TOC 4.9 ppm). The mineralization study was performed under UV + PMS and Vis + PMS, the previously identified optimal degradation conditions.

Both SnO_2-BiOI and TiO_2-BiOI demonstrated superior mineralization under UV + PMS compared to Vis + PMS, emphasizing the role of UV light in PMS activation (Fig. 4). The highest mineralization efficiency for both materials was observed in 5 ppm LAN solutions, reaching 91.7 ± 2.0 % (SnO_2-BiOI) and 98.2 ± 1.3 % (TiO_2-BiOI) under UV + PMS. However, under Vis + PMS, mineralization efficiency dropped, with TiO_2-BiOI showing a particularly significant decrease (47.8 %), suggesting a lower visible-light response for TiO_2-BiOI in PMS activation for LAN oxidation.

Interestingly, the multipollutant solution in tap water (MP-TAP) exhibited better mineralization than the same solution in Milli-Q water (MP-MQ). This effect was more pronounced for SnO_2-BiOI, where MP-TAP mineralization reached 85.7 ± 1.1 % (UV + PMS) and 76.5 ± 0.9 % (Vis + PMS), compared to MP-MQ (79.4 ± 2.0 % and 62.7 ± 1.2 %, respectively). This suggests that the presence of metal cations (e.g., Ca^{2+}, Mg^{2+}, Na^{+}) and anions (e.g., Cl^{-}, SO_4^{2-}) and natural organic matter in tap water may enhance PMS activation and radical generation, as reported in previous studies where ion-mediated PMS activation promoted hydroxyl and sulfate radical formation.

For TiO_2-BiOI, MP-TAP also exhibited enhanced mineralization, achieving 95.3 ± 1.4 % (UV + PMS) and 78.5 ± 0.4 % (Vis + PMS), further confirming the positive influence of natural water constituents on photocatalytic performance. However, its superior performance under UV light suggests that TiO_2-BiOI remains more efficient under high-energy irradiation conditions.

To further elucidate the influence of real water matrix constituents, we investigated the effect of various inorganic ions on photocatalytic mineralization in Milli-Q water supplemented with selected salts at environmentally relevant concentrations. As detailed in Tables S3 and S4, monovalent cations (Na^{+}, K^{+}) and common anions such as NO_3^{-} and SO_4^{2-} showed negligible impact on mineralization, while divalent cations (Ca^{2+}, Mg^{2+}) induced mild inhibition. Interestingly, bicarbonate (HCO_3^{-}) and phosphate (PO_4^{3-}) consistently enhanced mineralization across all concentrations and light conditions. These findings align with recent studies showing that carbonate and phosphate species can act as co-catalysts in PMS activation, improving degradation kinetics by expanding the oxidative route beyond hydroxyl and sulfate radicals. Additionally, Fe(III) and Cu(II) enhanced PMS activation and ROS generation, particularly under UV-A irradiation. These observations are

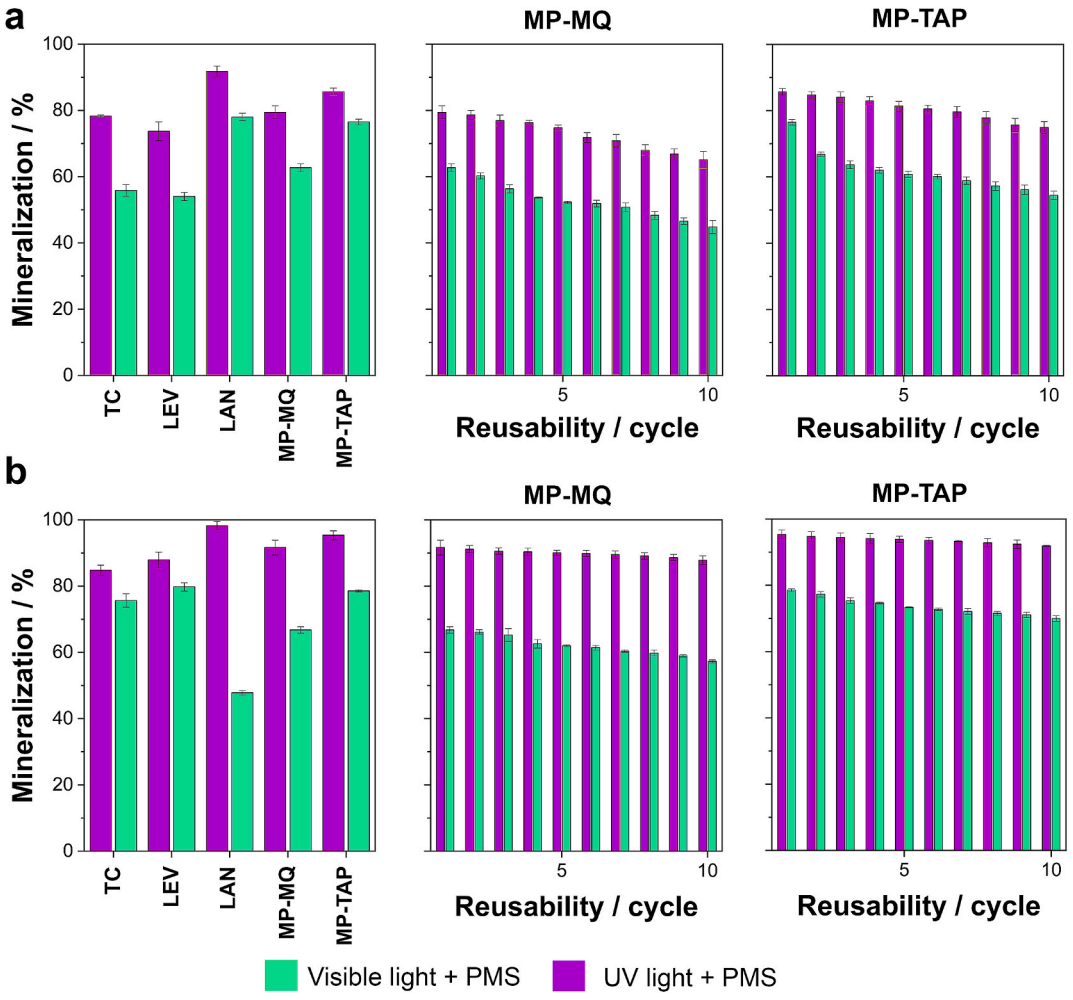

Fig. 4. Mineralization performance of (a) 5 nm SnO_2-BiOI and (b) 5 nm TiO_2-BiOI in different pollutant solutions. (Left): Comparison of mineralization efficiency in single-pollutant solutions of tetracycline (20 ppm), levofloxacin (20 ppm), and lansoprazole (5 ppm), as well as in multipollutant solutions prepared in Milli-Q water (MP-MQ) and filtered tap water (MP-TAP), containing tetracycline (10 ppm), levofloxacin (5 ppm), and lansoprazole (5 ppm). Experiments were conducted under UV light + PMS and visible light + PMS conditions for 90 min. (Center & right): Mineralization performance over 10 reusability cycles in multipollutant solutions, tested in Milli-Q water (center) and filtered tap water (right). All experiments were conducted in triplicate, and error bars represent standard deviations.

consistent with the improved mineralization noted in tap water, which contains natural levels of Ca^{2+}, Mg^{2+}, Na^{+}, Cl^{-}, and SO_4^{2-}. Collectively, these results emphasize the critical role of matrix composition in determining catalytic performance and support the applicability of BiOI-based heterostructures for real-world water treatment. Although specific ions at moderate to high concentrations may inhibit photocatalytic PMS mineralization in simplified systems, the natural ionic balance, buffering capacity, and presence of trace redox-active metals in tap water can synergistically enhance PMS activation and ROS-mediated degradation. This likely explains the superior mineralization observed in tap water compared to ultrapure Milli-Q water, highlighting the robustness and practical potential of the proposed heterostructured catalysts in complex environmental matrices [4,18,74–77].

A key factor in practical applications is catalyst stability over multiple cycles (Fig. 4). The reusability study revealed gradual efficiency losses over 10 cycles, with TiO_2-BiOI maintaining higher stability than SnO_2-BiOI. In MP-MQ, SnO_2-BiOI mineralization declined by 14.3 % (UV + PMS) and 17.8 % (Vis + PMS), while in MP-TAP, the losses were 10.8 % (UV + PMS) and 22 % (Vis + PMS). The greater decline in visible-light conditions suggests that photocorrosion or surface deactivation may be more prominent under lower-energy irradiation. In contrast, TiO_2-BiOI showed significantly lower losses, particularly under UV light (only 3.4 % in MP-TAP and 3.8 % in MP-MQ), reinforcing its long-term stability.

The lower stability of SnO_2-BiOI could be attributed to surface oxidation, leaching, or passivation effects, which are more pronounced in visible-light-driven reactions. TiO_2, known for its chemical robustness and resistance to photocorrosion, retained better activity even after prolonged cycling. The stability results align with prior studies, where Sn-based oxides demonstrated high initial activity but lower long-term stability compared to TiO_2-based systems.

These findings provide valuable insights for practical water treatment applications. The results demonstrate that UV + PMS activation remains the most effective approach for pollutant mineralization, reinforcing the potential of TiO_2-BiOI for high-efficiency, long-term use in advanced oxidation processes. However, SnO_2-BiOI exhibits promising adaptability for visible-light-driven mineralization, particularly in natural water matrices, where ionic species can enhance radical formation and improve efficiency. Furthermore, the observed mineralization enhancement in tap water highlights the need to consider water chemistry when designing photocatalytic treatment systems. The presence of alkalinity, hardness, and mineral ions may significantly influence PMS activation and pollutant degradation, suggesting that future research should focus on optimizing catalyst performance under complex environmental conditions.

To benchmark our materials against current photocatalysts, a comparative analysis is presented in **Table S5**, summarizing key performance metrics – including degradation efficiency, and mineralization – from recent PMS-based advanced oxidation systems [78,79]. Although direct comparisons must be made cautiously due to differences in experimental setups (e.g., pollutant type, initial concentration, light source, pH, catalyst dose, and PMS loading), this table offers a qualitative overview of the state-of-the-art. Remarkably, our Pd–SnO_2–BiOI and Pd–TiO_2–BiOI thin films exhibit superior or comparable mineralization degrees and degradation kinetics under both UV-A and visible-light conditions. In particular, their performance in real tap water matrices, without the need for pH adjustment, highlights their practical applicability and robustness. These findings confirm that the combination of ALD-engineered heterojunctions and PMS activation provides a highly competitive and scalable solution for the removal of emerging contaminants from aqueous environments.

3.3. Hydroxyl and sulfate radical generation of (Pd)-SnO_2-BiOI and (Pd)-TiO_2-BiOI thin films

Fig. 5 provides valuable insights into the generation of hydroxyl and sulfate radicals by BiOI-based heterojunction materials under dark conditions and UV and visible light irradiation, both in the presence and absence of 2.5 mM PMS. For these experiments, the SnO_2 and TiO_2 thickness was analyzed only for samples with a thickness of 5 nm.

The concentration of Ce(IV) serves as a quantitative measure of sulfate radical generation. As shown in Fig. 5**a**, PMS alone yields the lowest Ce(IV) concentration across all tested materials. Among them, BiOI exhibits the weakest performance, whereas Pd-SnO_2-BiOI achieves higher Ce(IV) concentration under the same conditions. This suggests that SnO_2 and Pd modifications significantly enhance BiOI's catalytic efficiency, even without light activation. The TiO_2-based composites (TiO_2-BiOI and Pd-TiO_2-BiOI) also exhibit higher Ce(IV) concentrations compared to unmodified BiOI, reinforcing the role of TiO_2 in facilitating redox reactions likely due to its superior electron mobility and oxidative properties.

When UV light is introduced alongside PMS, Ce(IV) concentrations increase significantly across all materials, confirming that UV irradiation effectively activates the photocatalysts. The Pd-TiO_2-BiOI composite produces the highest Ce(IV) concentration, followed closely by TiO_2-BiOI, suggesting that TiO_2 enhances photocatalytic oxidation under UV conditions due to its strong light absorption and efficient charge separation. Interestingly, Pd-SnO_2-BiOI, which demonstrated the highest Ce(IV) concentration with PMS alone, shows a slight decrease under UV irradiation. This implies that while SnO_2 enhances PMS activation, TiO_2-based materials perform better under UV exposure. Once again, BiOI alone remains the weakest performer, reaffirming its limited photocatalytic capability compared to heterojunction materials.

Under visible light with PMS, the performance trend shifts slightly, highlighting the influence of material composition on light absorption. TiO_2-BiOI continues to perform well, but Pd-SnO_2-BiOI surpasses Pd-TiO_2-BiOI, emerging as a strong competitor. This suggests that TiO_2 is highly effective under UV light, while SnO_2 and Pd modifications enhance visible-light response. However, Pd-TiO_2-BiOI, which excelled under UV, shows a decline in Ce(IV) concentration under visible light, possibly indicating that the TiO_2 phase is less effective in visible-light harvesting than SnO_2-based materials.

Overall, UV irradiation significantly enhances sulfate radical production compared to visible light, demonstrating the superior efficacy of UV light in directly cleaving the O–O bond in PMS, independent of the catalyst. The role of Pd in PMS activation is also crucial in understanding these trends. The Pd nanoparticle layer, particularly in its zero-valent state, can directly activate PMS through a redox cycle, wherein Pd(0) donates electrons to PMS, facilitating the formation of sulfate radicals. This mechanism mirrors other transition metal-mediated PMS activation systems, where electron transfer from the metal surface promotes PMS decomposition.

These findings highlight that Pd incorporation not only improves charge separation but also modulates ROS generation dynamics. The incorporation of Pd nanoparticles improved the long-term stability of BiOI-based photocatalysts, likely due to Schottky junction formation that enhances electron extraction and suppresses photocorrosion. However, their presence also altered the distribution of ROS, as supported by radical scavenging experiments (Fig. S8), where the quenching of $^{\bullet}OH$ and $SO_4^{\bullet -}$ showed distinct profiles compared to non-Pd systems. This suggests that Pd modifies the electron transfer pathways at the semiconductor surface, resulting in a shift in the dominant ROS generated during PMS activation under light irradiation. The suppression of hydroxyl radical production in Pd-containing catalysts, particularly under UV light, aligns with this mechanistic shift, further reinforcing Pd's distinct role in PMS activation.

The concentration of hTPA serves as a direct indicator of hydroxyl radical production. Higher hTPA concentrations correlate with greater hydroxyl radical generation, which is crucial for assessing the catalytic efficiency of these materials. As shown in Fig. 5**b**, when 2.5 mM of PMS is used alone, the lowest hTPA concentration is observed for BiOI, while Pd-SnO_2-BiOI exhibits the highest value. This suggests that BiOI alone

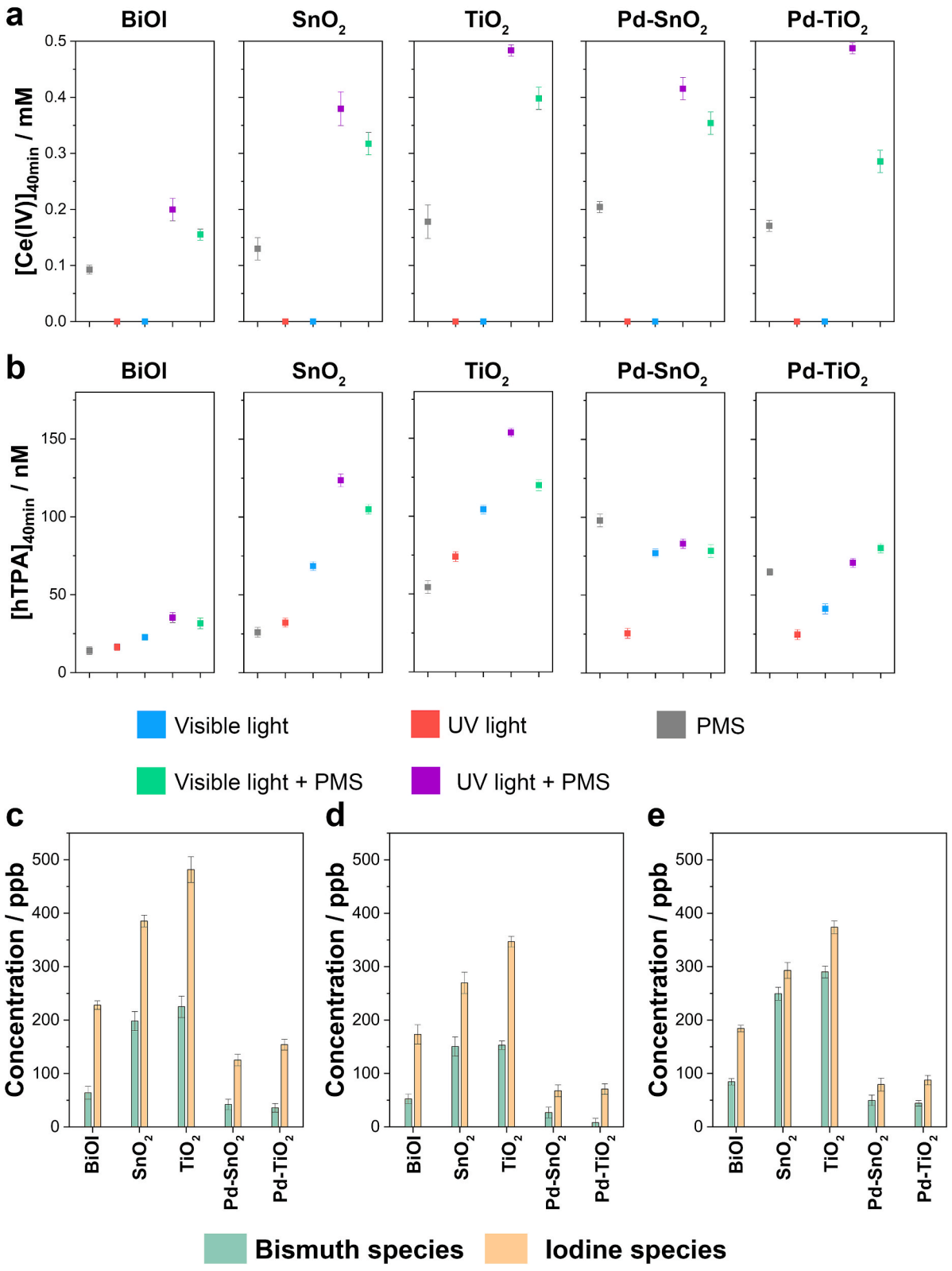

Fig. 5. (a) Cerium (IV) concentration in aqueous solution after 40 min of treatment, and (b) sodium hydroxyterephthalate (hTPA) concentration after 40 min under different conditions: PMS, UV irradiation, visible light irradiation, PMS + UV irradiation, and PMS + visible light irradiation, using BiOI, SnO_2-BiOI, TiO_2-BiOI, Pd-SnO_2-BiOI, and Pd-TiO_2-BiOI catalysts. Experimental conditions: $[PMS]_0 = 0$ or 2.5 mM, $[Ce(III)]_0 = 15$ mM or 0 mM, $[Na_2TPA]_0 = 0$ or 1 mM, and T = 25 °C. All experiments were performed in triplicate, with values reported as mean ± standard deviation. (c–e) Concentration of bismuth and iodine species in aqueous solution after 360 min of continuous visible light irradiation under different conditions: (c) no PMS or TC, (d) no PMS with 180 ppm TC, and (e) 2.5 mM PMS without TC. Results are presented as mean ± standard deviation from triplicate experiments.

has poor hydroxyl radical generation efficiency, whereas SnO_2 and Pd modifications significantly enhance PMS activation. Among TiO_2-based heterojunction materials, TiO_2-BiOI and Pd-TiO_2-BiOI outperform unmodified BiOI, underscoring TiO_2's critical role in hydroxyl radical generation. Pd-SnO_2-BiOI surpasses all other materials, suggesting that the synergistic effect of Pd and SnO_2 enhances PMS decomposition into hydroxyl radicals.

Under UV irradiation, hydroxyl radical formation increases for most materials, with TiO_2-BiOI displaying the highest hTPA concentration. This confirms that TiO_2 is highly effective in promoting hydroxyl radical generation under UV light due to its strong light absorption and efficient charge separation. SnO_2-BiOI also exhibits a noticeable increase, reinforcing its ability to activate PMS under UV conditions. However, Pd-SnO_2-BiOI and Pd-TiO_2-BiOI show decreased hTPA concentrations, suggesting a shift in reaction pathways. The presence of Pd likely promotes sulfate radical formation over hydroxyl radical production, thereby reducing hTPA levels under UV conditions.

Under visible light, hydroxyl radical formation increases substantially, particularly for TiO_2-BiOI and Pd-SnO_2-BiOI. The strong performance of TiO_2-BiOI suggests that TiO_2 modification enhances visible-light absorption and electron-hole pair separation, leading to more efficient hydroxyl radical production. Additionally, SnO_2-BiOI and Pd-TiO_2-BiOI show significant improvements under visible light, indicating that SnO_2 and Pd modifications enhance visible-light-driven hydroxyl radical formation. However, BiOI alone still exhibits the weakest performance, confirming its limited photocatalytic efficiency.

The findings indicate that TiO_2 and SnO_2 modifications substantially enhance hydroxyl radical production under both UV and visible light irradiation, particularly when combined with PMS. The highest hTPA concentrations are observed for TiO_2-BiOI and SnO_2-BiOI, confirming their superior hydroxyl radical generation ability. Meanwhile, Pd-containing catalysts show lower hydroxyl radical production under UV light, likely due to their tendency to promote sulfate radical formation instead. However, Pd modification enhances visible-light-driven hydroxyl radical generation, demonstrating its role in altering reaction pathways depending on the irradiation source.

Overall, TiO_2-BiOI emerges as the most efficient material for hydroxyl radical generation, particularly under UV + PMS conditions, whereas BiOI alone remains the least effective. This highlights the importance of rational heterojunction design in optimizing photocatalytic PMS activation. This highlights the importance of rational heterojunction design in optimizing photocatalytic PMS activation. Specific radical scavenger experiments were not conducted, but the use of real tap water – containing natural scavengers such as bicarbonate and chloride – provided an inherently competitive environment that supports the formation of reactive species under visible light. The observed degradation and mineralization efficiencies under these conditions further confirm the role of PMS-activated radicals in pollutant removal.

These results further confirm that: (i) UV light is superior for sulfate radical production, whereas visible light is more effective for hydroxyl radical generation; (ii) Pd-SnO_2-BiOI is the most efficient catalyst for UV-driven PMS activation, maximizing sulfate radical formation through charge separation and Pd-assisted PMS decomposition; (iii) TiO_2-BiOI and SnO_2-BiOI show the highest visible light-driven hydroxyl radical production, benefiting from their type-II band alignments; and (iv) Pd incorporation enhances electron transfer but redirects the reaction pathway toward sulfate radicals at the expense of hydroxyl radical formation. The study provides valuable insights into the role of ALD-engineered BiOI-based heterojunctions in PMS activation. Future research should focus on enhancing hydroxyl radical production in Pd-modified systems while maintaining their improved charge separation and stability, potentially by optimizing Pd loading or integrating co-catalysts that favor hydroxyl radical generation. Although specific EPR or quenching tests for species such as $O_2^{\bullet-}$, $HO_2^{\bullet-}$, e^-, h^+, and $^1O_2$ were not conducted, previous studies suggest their potential involvement in PMS-based systems. The observed photocatalytic activity under complex tap water matrices, combined with the successful degradation and mineralization results, support the participation of multiple ROS including $SO_5^{\bullet-}$ and $^1O_2$. Recent works [80,81] have also highlighted the significance of these species in similar PMS activation systems and justify their likely presence in our system.

3.4. Photostability of (Pd)-SnO_2-BiOI and (Pd)-TiO_2-BiOI thin films

The photostability of BiOI-based thin films is a crucial factor in determining their long-term applicability in catalytic water treatment. One of the primary limitations of BiOI as a photocatalyst is its susceptibility to photocorrosion, mainly due to iodide oxidation and the subsequent leaching of iodine species into the solution. This process leads to structural degradation and a decline in catalytic efficiency over time. This section analyses the photostability of Pd-modified SnO_2-BiOI and TiO_2-BiOI thin films, focusing on the leaching of bismuth and iodine species under visible and UV irradiation, both in the presence and absence of organic pollutants and/or PMS.

To assess the intrinsic photostability of the synthesized catalysts, thin films were tested in pure water (without PMS or organic pollutants). The extent of photocorrosion was determined by measuring the release of bismuth and iodine species into the solution after 360 min of visible light and UV exposure. As shown in Fig. 5c, pristine BiOI exhibited moderate photocorrosion. In contrast, under visible light irradiation, unmodified SnO_2-BiOI and TiO_2-BiOI films suffered significantly higher levels of photocorrosion, with bismuth concentrations reaching 198 ± 18 ppb (SnO_2-BiOI) and 225 ± 20 ppb (TiO_2-BiOI), while iodine species increased to 385 ± 11 ppb and 482 ± 24 ppb, respectively. Notably, under UV irradiation, the same trend was observed, albeit with lower leaching. These findings suggest that, despite improving charge separation, the addition of SnO_2 and TiO_2 alone does not effectively mitigate photocorrosion. To further evaluate the stability of the heterostructures and the risk of secondary environmental contamination, the leaching of Sn and Ti ions was also quantified under the same irradiation conditions. The results indicated that Sn(IV) and Ti(IV) concentrations in solution remained below 4 % of the total deposited oxide content after 360 min, confirming that although Bi and I leaching dominates, minor release of Sn and Ti does occur. However, Pd incorporation significantly enhanced photostability. Pd-SnO_2-BiOI exhibited a remarkable reduction in leaching, while Pd-TiO_2-BiOI showed the lowest levels of bismuth and iodine species. In addition, Pd deposition further suppressed Sn and Ti ion leaching, maintaining metal release well below levels considered critical for secondary contamination. These results confirm that Pd acts as an electron sink, stabilizing the material and reducing self-oxidation, thereby mitigating photocorrosion.

As illustrated in Fig. 5d, the presence of an organic pollutant (180 ppm of TC) in the solution further influenced photocorrosion behavior. The pollutant reduced BiOI degradation, likely due to competitive interactions between organic species and photogenerated holes, which limited direct iodide oxidation. Similarly, SnO_2-BiOI and TiO_2-BiOI exhibited high photocorrosion levels, reaffirming that unmodified heterojunctions do not effectively suppress degradation. Conversely, Pd-SnO_2-BiOI and Pd-TiO_2-BiOI demonstrated superior stability, reinforcing the critical role of Pd in preserving BiOI integrity, even in the presence of competing organic molecules.

The addition of 2.5 mM PMS into the solution resulted in increased BiOI degradation for most samples (Fig. 5e). The oxidative environment generated by PMS facilitated the formation of reactive sulfate radicals, which contributed to BiOI oxidation. Pristine BiOI exhibited a notable rise in photocorrosion, while SnO_2-BiOI and TiO_2-BiOI displayed severe degradation, confirming that although these heterojunctions enhance photocatalytic efficiency, they fail to protect BiOI from oxidative degradation under PMS activation. In stark contrast, Pd-SnO_2-BiOI and Pd-TiO_2-BiOI demonstrated remarkable resistance to photocorrosion. The improved stability of Pd-modified heterojunctions suggests that Pd

plays a dual role: (i) suppressing direct BiOI oxidation by scavenging photogenerated electrons; and (ii) promoting an alternative reaction pathway, where PMS activation occurs on Pd sites rather than through BiOI self-oxidation.

A comparative analysis of the different experimental conditions confirms that Pd-SnO_2-BiOI and Pd-TiO_2-BiOI are significantly more stable than their Pd-free counterparts, with Pd-TiO_2-BiOI exhibiting the lowest photocorrosion rates. The presence of Pd effectively mitigates iodine leaching and bismuth dissolution, thereby enhancing the longevity of the photocatalyst. Crucially, the reduced leaching of Sn and Ti from Pd-modified films minimizes the risk of secondary metal ion contamination, supporting the environmental safety and practical viability of these materials in real water treatment applications. These findings underscore the importance of Pd modification in preventing BiOI degradation, ensuring structural stability, and prolonging photocatalytic activity.

4. Conclusions

This work demonstrates the rational design of SnO_2- and TiO_2-modified BiOI thin films via atomic layer deposition (ALD) for enhanced light-driven PMS-activated pollutant mineralization. The formation of SnO_2-BiOI and TiO_2-BiOI heterojunctions improved charge separation and reactive radical generation, enabling superior photocatalytic performance compared to pristine BiOI.

Under UV + PMS conditions, TiO_2-BiOI achieved the highest efficiency, with 92.7 % tetracycline degradation and 84.8 % mineralization after 90 min, while SnO_2-BiOI showed superior activity under visible + PMS irradiation, achieving 80.8 % degradation and 76.5 % mineralization. Pd nanoparticle deposition enhanced photostability by reducing photocorrosion but selectively altered the PMS activation mechanism, favoring sulfate radical production and benefiting SnO_2-based systems under visible light. In contrast, Pd addition negatively affected TiO_2-BiOI performance under UV irradiation.

The stability of TiO_2-BiOI was superior, retaining >95 % activity after 10 cycles, while SnO_2-BiOI displayed enhanced reactivity in visible-light-driven processes, particularly in tap water matrices where dissolved ions facilitated PMS activation. The results position TiO_2-BiOI as the most suitable catalyst for UV-assisted applications, while Pd-SnO_2-BiOI is more appropriate for visible-light-driven processes.

These results underscore the potential of ALD-engineered BiOI-based heterojunctions for scalable and sustainable wastewater treatment. The rational combination of semiconductors enables the development of highly efficient catalysts with improved charge separation, photostability, and pollutant degradation capabilities. The ability to precisely tune material properties through ALD allows for tailored photocatalyst design, making this approach a viable strategy for addressing emerging contaminants in diverse water matrices. Moreover, the integration of PMS activation with visible-light-driven photocatalysis offers a sustainable and cost-effective alternative to conventional water treatment technologies, particularly for recalcitrant organic pollutants. Although a full economic assessment is beyond the scope of this work, the use of low-cost, earth-abundant materials (BiOI, SnO_2, TiO_2) combined with nanoscale ALD engineering offers a promising route toward economically viable catalysts. The high reusability, minimal material consumption due to thin-film design, and enhanced stability further support the potential for long-term cost-effectiveness in real water treatment systems.

Future research should focus on further optimizing catalyst composition, exploring alternative co-catalyst modifications, and extending the approach to additional contaminants. Investigating long-term catalyst stability under continuous flow conditions, as well as the impact of real wastewater matrices, will be crucial for practical implementation. The findings of this study provide a strong foundation for the advancement of advanced oxidation processes, paving the way for next-generation photocatalytic materials capable of addressing global water pollution challenges in a scalable and efficient manner.

CRediT authorship contribution statement

Laura Huidobro: Writing – original draft, Methodology, Investigation, Formal analysis, Data curation, Conceptualization. **Mahmoud Abid:** Writing – original draft, Methodology, Investigation, Formal analysis, Data curation, Conceptualization. **Haitham Maslouh:** Writing – original draft, Methodology, Investigation, Formal analysis, Data curation, Conceptualization. **Arnaud Demore:** Writing – original draft, Methodology, Investigation, Formal analysis, Data curation, Conceptualization. **Mikhael Bechelany:** Writing – review & editing, Writing – original draft, Validation, Supervision, Project administration, Methodology, Investigation, Funding acquisition, Formal analysis, Conceptualization. **Elvira Gómez:** Writing – original draft, Supervision, Project administration, Methodology, Investigation, Funding acquisition, Formal analysis, Conceptualization. **Albert Serrà:** Writing – review & editing, Writing – original draft, Supervision, Project administration, Methodology, Investigation, Funding acquisition, Formal analysis, Data curation, Conceptualization.

Declaration of competing interest

The authors declare that they have no known competing financial interests or personal relationships that could have appeared to influence the work reported in this paper.

Acknowledgement

This work was supported by Grant Project PID2020-115663 GB-C32, funded by MICIU/AEI/10.13039/501100011033. L. H. also acknowledge the predoctoral fellowship PREDOCS-UB 2021 provided by the University of Barcelona. The authors express their gratitude to CCiT-UB for providing access to their equipment.

Appendix A. Supplementary data

Supplementary data to this article can be found online at https://doi.org/10.1016/j.matdes.2025.114375.

Data availability

Data will be made available on request.

References

[1] K. Kulik, A. Lenart-Boroń, K. Wyrzykowska, Impact of antibiotic pollution on the bacterial population within surface water with special focus on mountain rivers, Water (Switzerland) 15 (2023) 1–25, https://doi.org/10.3390/w15050975.
[2] P. Rzymski, W. Gwenzi, B. Poniedziałek, S. Mangul, A. Fal, Climate warming, environmental degradation and pollution as drivers of antibiotic resistance, Environ. Pollut. 346 (2024), https://doi.org/10.1016/j.envpol.2024.123649.
[3] A. Gupta, S. Kumar, Y. Bajpai, K. Chaturvedi, P. Johri, R.K. Tiwari, V. Vivekanand, M. Trivedi, Pharmaceutically active micropollutants: Origin, hazards and removal, Front. Microbiol. 15 (2024), https://doi.org/10.3389/fmicb.2024.1339469.
[4] A. Serrà, E. Gómez, N. al Hoda al Bast, Y. Zhang, M. Duque, M. José Esplandiu, J. Esteve, J. Nogués, B. Sepúlveda, Wireless pulsed nanophotoelectrochemical cell for the ultrafast degradation of organic pollutants, Chem. Eng. J. 487 (2024), https://doi.org/10.1016/j.cej.2024.150663.
[5] M.R. Landsman, R. Sujanani, S.H. Brodfuehrer, C.M. Cooper, A.G. Darr, R.J. Davis, K. Kim, S. Kum, L.K. Nalley, S.M. Nomaan, C.P. Oden, A. Paspureddi, K. K. Reimund, L.S. Rowles, S. Yeo, D.F. Lawler, B.D. Freeman, L.E. Katz, Water treatment: Are membranes the panacea? Annu. Rev. Chem. Biomol. Eng. 11 (2020) 559–585, https://doi.org/10.1146/annurev-chembioeng-111919-091940.
[6] C.X. Hiller, U. Hübner, S. Fajnorova, T. Schwartz, J.E. Drewes, Antibiotic microbial resistance (AMR) removal efficiencies by conventional and advanced wastewater treatment processes: A review, Sci. Total Environ. 685 (2019) 596–608, https://doi.org/10.1016/j.scitotenv.2019.05.315.
[7] A. Serrà, L. Philippe, F. Perreault, S. Garcia-Segura, Photocatalytic treatment of natural waters. Reality or hype? The case of cyanotoxins remediation, Water Res. 188 (2021), https://doi.org/10.1016/j.watres.2020.116543.

[8] E. Edefell, P. Falås, E. Torresi, M. Hagman, M. Cimbritz, K. Bester, M. Christensson, Promoting the degradation of organic micropollutants in tertiary moving bed biofilm reactors by controlling growth and redox conditions, J. Hazard. Mater. 414 (2021) 125535, https://doi.org/10.1016/j.jhazmat.2021.125535.

[9] R. Cestaro, L. Philippe, A. Serrà, E. Gómez, P. Schmutz, Electrodeposited manganese oxides as efficient photocatalyst for the degradation of tetracycline antibiotics pollutant, Chem. Eng. J. 462 (2023), https://doi.org/10.1016/j.cej.2023.142202.

[10] S. Raza, E. Ghasali, Y. Orooji, H. Lin, C. Karaman, E.N. Dragoi, N. Erk, Two dimensional (2D) materials and biomaterials for water desalination; structure, properties, and recent advances, Environ. Res. 219 (2023) 114998, https://doi.org/10.1016/j.envres.2022.114998.

[11] I. Ali, O.M.L. Alharbi, A. Tkachev, E. Galunin, A. Burakov, V.A. Grachev, Water treatment by new-generation graphene materials: hope for bright future, Environ. Sci. Pollut. Res. 25 (2018) 7315–7329, https://doi.org/10.1007/s11356-018-1315-9.

[12] J. Li, S. Yan, J. Wu, Q. Cheng, K. Wang, Improving hydrogen peroxide photosynthesis over inorganic/organic S-scheme photocatalyst with $LiFePO_4$, Acta Physico-Chimica Sin. 41 (2025) 100104, https://doi.org/10.1016/j.actphy.2025.100104.

[13] X. Liu, Z. Yang, H. Liu, Y. Li, G. Zhang, Efficient photocatalytic degradation of microplastics by constructing a novel Z-scheme Fe-doped BiO_{2-x}/BiOI heterojunction with full-spectrum response: Mechanistic insights and theory calculations, J. Hazard. Mater. 480 (2024) 1–9, https://doi.org/10.1016/j.jhazmat.2024.136080.

[14] A.K. Pandey, R. Reji Kumar, I.A. Laghari, M. Samykano, R. Kothari, A. M. Abusorrah, K. Sharma, V.V. Tyagi, Utilization of solar energy for wastewater treatment: Challenges and progressive research trends, J. Environ. Manage. 297 (2021) 113300, https://doi.org/10.1016/j.jenvman.2021.113300.

[15] E. Gómez, R. Cestaro, L. Philippe, A. Serrà, Electrodeposition of nanostructured Bi_2MoO_6@Bi_2MoO_{6-x} homojunction films for the enhanced visible-light-driven photocatalytic degradation of antibiotics, Appl. Catal. B Environ. 317 (2022), https://doi.org/10.1016/j.apcatb.2022.121703.

[16] A. Aranda-Aguirre, D. Valdivia-Alvarez, E.C. Pastrana, S. Garcia-Segura, G. A. Cerrón-Calle, H. Alarcon, Engineered controlled on the synthesis of bismuth-molybdenum oxide semiconductors tailors photoelectrocatalytic activity, J. Electroanal. Chem. 980 (2025) 118956, https://doi.org/10.1016/j.jelechem.2025.118956.

[17] R.J.A. Felisardo, E. Brillas, E. Bezerra Cavalcanti, S. Garcia-Segura, Revealing degradation of organic constituents of urine during the electrochemical oxidation of ciprofloxacin via boron-doped diamond anode, Sep. Purif. Technol. 331 (2024) 125655, https://doi.org/10.1016/j.seppur.2023.125655.

[18] W. Wang, Z. Yang, Y. Li, J. Wang, G. Zhang, Enhanced peroxymonosulfate activation by copper-doped bismuth oxides for the efficient photo-degradation of ciprofloxacin: Crucial role of copper sites, theoretical calculation and mechanism insight, Environ. Sci. Nano (2024) 1545–1557, https://doi.org/10.1039/d4en00994k.

[19] E. Gómez, A. Fons, R. Cestaro, A. Serrà, Enhanced activation of peroxymonosulfate for tetracycline degradation using CoNi-based electrodeposited films, Nanomaterials 13 (2023) 1–19, https://doi.org/10.3390/nano13050790.

[20] Y. Yu, P. Li, B. Zhu, Y. Liu, R. Yu, S. Ge, The application of sulfate radical-based advanced oxidation processes in hydrothermal treatment of activated sludge at different stages: A comparative study, Environ. Sci. Pollut. Res. 29 (2022) 59456–59465, https://doi.org/10.1007/s11356-022-20038-y.

[21] M. Manna, S. Sen, Advanced oxidation process: a sustainable technology for treating refractory organic compounds present in industrial wastewater, Environ. Sci. Pollut. Res. 30 (2023) 25477–25505, https://doi.org/10.1007/s11356-022-19435-0.

[22] A. Saravanan, V.C. Deivayanai, P.S. Kumar, G. Rangasamy, R.V. Hemavathy, T. Harshana, N. Gayathri, K. Alagumalai, A detailed review on advanced oxidation process in treatment of wastewater: Mechanism, challenges and future outlook, Chemosphere 308 (2022) 136524, https://doi.org/10.1016/j.chemosphere.2022.136524.

[23] N. Tian, Z. Madani, S. Giannakis, A.A. Isari, M. Arjmand, F. Hasanvandian, M. Noorisepehr, B. Kakavandi, Peroxymonosulfate assisted pesticide breakdown: Unveiling the potential of a novel S-scheme ZnO@$CoFe_2O_4$ photo-catalyst, anchored on activated carbon, Environ. Pollut. 334 (2023) 122059, https://doi.org/10.1016/j.envpol.2023.122059.

[24] B. Kakavandi, M. Zehtab Salmasi, M. Ahmadi, A. Naderi, P. Roccaro, J. Bedia, M. Hasham Firooz, R., Rezaei Kalantary, Spinel cobalt ferrite-based porous activated carbon in conjunction with UV light irradiation for boosting peroxymonosulfate oxidation of bisphenol A, J. Environ. Manage. 342 (2023) 118242, https://doi.org/10.1016/j.jenvman.2023.118242.

[25] Q. Cheng, J. Li, Y. Huang, X. Liu, B. Zhou, Q. Xiong, K. Wang, Verifying the unique charge migration pathway in polymeric homojunctions for artificial photosynthesis of hydrogen peroxide, Adv. Sci. 2500218 (2025) 1–10, https://doi.org/10.1002/advs.202500218.

[26] K. Wang, Y. Hu, X. Liu, J. Li, B. Liu, Visible-light-driven CO_2 photoreduction over atomically strained indium sites in ambient air, Nat. Commun. 16 (2025) 1–9, https://doi.org/10.1038/s41467-025-57140-x.

[27] L. Huidobro, Q. Bautista, M. Alinezhadfar, E. Gómez, A. Serrà, Enhanced visible-light-driven peroxymonosulfate activation for antibiotic mineralization using electrosynthesized nanostructured bismuth oxyiodides thin films, J. Environ. Chem. Eng. 12 (2024), https://doi.org/10.1016/j.jece.2024.112545.

[28] S. Luo, J. Chen, Z. Huang, C. Liu, M. Fang, Controllable synthesis of Titania-supported bismuth oxyiodide heterostructured nanofibers with highly exposed (1 1 0) bismuth oxyiodide facets for enhanced photocatalytic activity, ChemCatChem 8 (2016) 3780–3789, https://doi.org/10.1002/cctc.201601047.

[29] A.C. Mera, C.A. Rodríguez, M.F. Meléndrez, H. Valdés, Synthesis and characterization of BiOI microspheres under standardized conditions, J. Mater. Sci. 52 (2017) 944–954, https://doi.org/10.1007/s10853-016-0390-x.

[30] Z. Zhan, F. Wei, J. Zheng, C. Yin, W. Yang, L. Yao, S. Tang, D. Liu, Visible light driven recyclable micromotors for “on-the-fly” water remediation, Mater. Lett. 258 (2020) 126825, https://doi.org/10.1016/j.matlet.2019.126825.

[31] L. Huidobro, A. Domingo, E. Gómez, A. Serrà, Bismuth oxyiodide-based composites for advanced visible-light activation of peroxymonosulfate in pharmaceutical mineralization, Chemosphere 366 (2024) 143532, https://doi.org/10.1016/j.chemosphere.2024.143532.

[32] L. Hao, P. Ju, Y. Zhang, X. Zhai, C. Sun, J. Duan, Fabrication of hierarchical flower-like BiOI/MoS_2 heterostructures with highly enhanced visible-light photocatalytic activities, Colloids Surf. A. 610 (2021) 125714, https://doi.org/10.1016/j.colsurfa.2020.125714.

[33] G. Tekin, G. Ersöz, S. Atalay, Comparison of synthesis methods for BiOI/g-C3N4 heterojunction photocatalysts and testing their visible light activity in sugar processing wastewater treatment, J. Ind. Eng. Chem. 126 (2023) 292–306, https://doi.org/10.1016/j.jiec.2023.06.020.

[34] A.A. Putri, S. Kato, N. Kishi, T. Soga, Study of annealing temperature effect on the photovoltaic performance of BiOI-based materials, Appl. Sci. 9 (2019), https://doi.org/10.3390/app9163342.

[35] R.M. Matiur, A.A. Abuelwafa, A.A. Putri, S. Kato, N. Kishi, T. Soga, Annealing effects on structural and photovoltaic properties of the dip-SILAR-prepared bismuth oxyhalides (BiOI, $Bi_7O_9I_3$, Bi_5O_7I) films, SN Appl. Sci. 3 (2021) 1–11, https://doi.org/10.1007/s42452-021-04153-y.

[36] R.M. Matiur, A.A. Abuelwafa, S. Kato, N. Kishi, T. Soga, A comparative study on optical properties of BiOI, $Bi_7O_9I_3$ and Bi_5O_7I materials, Opt. Mater. (Amst). 111 (2021) 110677, https://doi.org/10.1016/j.optmat.2020.110677.

[37] C. Liu, X.J. Wang, Room temperature synthesis of $Bi_4O_5I_2$ and Bi_5O_7I ultrathin nanosheets with a high visible light photocatalytic performance, Dalt. Trans. 45 (2016) 7720–7727, https://doi.org/10.1039/c6dt00530f.

[38] H. Chen, Y. Hu, Z. Ying, Y. Xia, J. Ye, J. Zhao, S. Zhang, BiOI-SnO_2 heterojunction design to boost visible-light-driven photocatalytic NO purification, Int. J. Environ. Res. Public Health 20 (2023), https://doi.org/10.3390/ijerph20054009.

[39] X. Liao, T.-T. Li, H.-T. Ren, X. Zhang, B. Shen, J.-H. Lin, C.-W. Lou, Construction of BiOI/TiO_2 flexible and hierarchical S-scheme heterojunction nanofibers membranes for visible-light-driven photocatalytic pollutants degradation, Sci. Total Environ. 806 (2022) 150698, https://doi.org/10.1016/j.scitotenv.2021.150698.

[40] B. Ogoh-Orch, P. Keating, A. Ivaturi, Visible-light-active BiOI/TiO_2 heterojunction photocatalysts for remediation of crude oil-contaminated water, ACS Omega 8 (2023) 43556–43572, https://doi.org/10.1021/acsomega.3c04359.

[41] Y. Chen, J. Huang, J. Zhong, M. Li, Z. Li, C. Yang, Enhanced photocatalytic performance of TiO_2/BiOI heterojunctions benefited from effective separation of photogenerated carriers, Chem. Phys. Lett. 780 (2021) 138966, https://doi.org/10.1016/j.cplett.2021.138966.

[42] Y.Q. Cao, J. Chen, H. Zhou, L. Zhu, X. Li, Z.Y. Cao, D. Wu, A.D. Li, Photocatalytic activity and photocorrosion of atomic layer deposited ZnO ultrathin films for the degradation of methylene blue, Nanotechnology 26 (2015), https://doi.org/10.1088/0957-4484/26/2/024002.

[43] H. Wang, C. Zhang, X. Zhang, S. Wang, Z. Xia, G. Zeng, J. Ding, N. Ren, Construction of Fe_3O_4@β-CD/g-C_3N_4 nanocomposite catalyst for degradation of PCBs in wastewater through photodegradation and heterogeneous Fenton oxidation, Chem. Eng. J. 429 (2022) 132445, https://doi.org/10.1016/j.cej.2021.132445.

[44] N. Li, J. Zhang, Y. Tian, J. Zhao, J. Zhang, W. Zuo, Precisely controlled fabrication of magnetic 3D γ-Fe_2O_3@ZnO core-shell photocatalyst with enhanced activity: Ciprofloxacin degradation and mechanism insight, Chem. Eng. J. 308 (2017) 377–385, https://doi.org/10.1016/j.cej.2016.09.093.

[45] M.J. Mortelliti, C.W. Huang, J.M. Atkin, J.L. Dempsey, Mixed Tin-titanium oxides by atomic layer deposition on planar substrates: Physical and electronic structure, Appl. Surf. Sci. 573 (2022) 151564, https://doi.org/10.1016/j.apsusc.2021.151564.

[46] D.R. Miller, S.A. Akbar, P.A. Morris, Nanoscale metal oxide-based heterojunctions for gas sensing: A review, Sensors Actuators, B Chem. 204 (2014) 250–272, https://doi.org/10.1016/j.snb.2014.07.074.

[47] C. Liu, S. Mao, H. Wang, Y. Wu, F. Wang, M. Xia, Q. Chen, Peroxymonosulfate-assisted for facilitating photocatalytic degradation performance of 2D/2D WO_3/BiOBr S-scheme heterojunction, Chem. Eng. J. 430 (2022), https://doi.org/10.1016/j.cej.2021.132806.

[48] Y. Peng, H. Shi, Z. Wang, Y. Fu, Y. Liu, Kinetics and reaction mechanism of photochemical degradation of diclofenac by UV-activated peroxymonosulfate, RSC Adv. 11 (2021) 6804–6817, https://doi.org/10.1039/d0ra10178h.

[49] S. Wacławek, H.V. Lutze, K. Grübel, V.V.T. Padil, M. Černík, D.D. Dionysiou, Chemistry of persulfates in water and wastewater treatment: A review, Chem. Eng. J. 330 (2017) 44–62, https://doi.org/10.1016/j.cej.2017.07.132.

[50] Z. Sun, X. Liu, X. Dong, X. Zhang, Y. Tan, F. Yuan, S. Zheng, C. Li, Synergistic activation of peroxymonosulfate via in situ growth $FeCo_2O_4$ nanoparticles on natural rectorite: Role of transition metal ions and hydroxyl groups, Chemosphere 263 (2021) 127965, https://doi.org/10.1016/j.chemosphere.2020.127965.

[51] M. Ortiz, E. Gómez, A. Serrà, Recyclable biomimetic sunflower pollen-based photocatalyst for enhanced degradation of pharmaceuticals, Small 2405204 (2024) 1–13, https://doi.org/10.1002/smll.202405204.

[52] R. Bujaldón, M. Benamara, R. Dhahri, E. Gómez, A. Serrà, Attuning doped ZnO-based composites for an effective light-driven mineralization of pharmaceuticals via PMS activation, Chemosphere 357 (2024), https://doi.org/10.1016/j.chemosphere.2024.142127.
[53] C. Wang, Y. Li, L. Huang, L. Yang, H. Wang, J. Liu, J. Liu, Z. Song, L. Huang, Enhanced photocatalytic antibacterial and degradation performance by n-p type 0D/2D SnO_{2-x}/BiOI photocatalyst under LED light, Chem. Eng. J. 411 (2021) 128505, https://doi.org/10.1016/j.cej.2021.128505.
[54] S. Rajasri, S. Kalikeri, S. Balachandran, K. Gowthami, G. Thirunarayanan, M. Swaminathan, I. Muthuvel, Enhanced photodegradation of 2,4-dinitrophenol by n–p type TiO_2/BiOI nanocomposite, J. Indian Chem. Soc. 99 (2022) 100337, https://doi.org/10.1016/j.jics.2021.100337.
[55] C. Badie, M. Drobek, A. Julbe, C. Charmette, J. Cartier, J.M. Decams, V. Astie, M. Bechelany, L. Santinacci, Development of hydrogen-selective TiO_xNy-Pd composite membrane materials by atomic layer deposition, Appl. Mater. Today 39 (2024) 1–10, https://doi.org/10.1016/j.apmt.2024.102303.
[56] C. Badie, J.H. Lee, A. Mirzaei, H.W. Kim, S. Sayegh, M. Bechelany, L. Santinacci, S. S. Kim, Enhanced sensitivity towards hydrogen by a TiN interlayer in Pd-decorated SnO_2 nanowires, J. Mater. Chem. A 11 (2023) 12202–12213, https://doi.org/10.1039/d3ta00020f.
[57] S. Sayegh, F. Tanos, A. Nada, G. Lesage, F. Zaviska, E. Petit, V. Rouessac, I. Iatsunskyi, E. Coy, R. Viter, D. Damberga, M. Weber, A. Razzouk, J. Stephan, M. Bechelany, Tunable TiO2-BN-Pd nanofibers by combining electrospinning and atomic layer deposition to enhance photodegradation of acetaminophen, Dalt. Trans. 51 (2022) 2674–2695, https://doi.org/10.1039/d1dt03715c.
[58] S. Sayegh, M. Abid, F. Tanos, M. Cretin, G. Lesage, F. Zaviska, E. Petit, B. Navarra, I. Iatsunskyi, E. Coy, R. Viter, V. Fedorenko, A. Ramanavicius, A. Razzouk, J. Stephan, M. Bechelany, N-doped TiO2 nanotubes synthesized by atomic layer deposition for acetaminophen degradation, Colloids Surf. A Physicochem. Eng. Asp. 655 (2022) 130213, https://doi.org/10.1016/j.colsurfa.2022.130213.
[59] A. Merenda, M. Weber, M. Bechelany, F.-M. Allioux, L. Hyde, L. Kong, L.F. Dumée, Fabrication of Pd-TiO_2 nanotube photoactive junctions via Atomic Layer Deposition for persistent pesticide pollutants degradation, Appl. Surf. Sci. 483 (2019) 219–230, https://doi.org/10.1016/j.apsusc.2019.03.285.
[60] S.E. Page, W.A. Arnold, K. McNeill, Terephthalate as a probe for photochemically generated hydroxyl radical, J. Environ. Monit. 12 (2010) 1658–1665, https://doi.org/10.1039/c0em00160k.
[61] A. Crovetto, A. Hajijafarassar, O. Hansen, B. Seger, I. Chorkendorff, P.C.K. Vesborg, Parallel Evaluation of the BiI_3, BiOI, and Ag_3BiI_6Layered Photoabsorbers, Chem. Mater. 32 (2020) 3385–3395, https://doi.org/10.1021/acs.chemmater.9b04925.
[62] E.A. Abdullah, Band edge positions as a key parameter to a systematic design of heterogeneous photocatalyst, Eur. J. Chem. 10 (2019) 82–94, https://doi.org/10.5155/eurjchem.10.1.82-94.1809.
[63] Z.-K. Tang, W.-J. Yin, L. Zhang, B. Wen, D.-Y. Zhang, L.-M. Liu, W.-M. Lau, Spatial separation of photo-generated electron-hole pairs in BiOBr/BiOI bilayer to facilitate water splitting, Sci. Rep. 6 (2016) 32764, https://doi.org/10.1038/srep32764.
[64] Z. Kerrami, A. Sibari, O. Mounkachi, A. Benyoussef, M. Benaissa, Improved photo-electrochemical properties of strained SnO_2, Int. J. Hydrogen Energy 45 (2020) 11035–11039, https://doi.org/10.1016/j.ijhydene.2018.03.199.
[65] O. Mounkachi, E. Salmani, M. Lakhal, H. Ez-Zahraouy, M. Hamedoun, M. Benaissa, A. Kara, A. Ennaoui, A. Benyoussef, Band-gap engineering of SnO_2, Sol. Energy Mater. Sol. Cells 148 (2016) 34–38, https://doi.org/10.1016/j.solmat.2015.09.062.
[66] A.M. Ganose, D.O. Scanlon, Band gap and work function tailoring of SnO_2 for improved transparent conducting ability in photovoltaics, J. Mater. Chem. C 4 (2016) 1467–1475, https://doi.org/10.1039/c5tc04089b.
[67] M. Abid, T.M. Howayek, O. Mazur, R. Viter, M.F. Bekheet, A.A. Nada, D. Bezzerga, J. Hong, P. Miele, I. Iatsunskyi, E. Coy, G. Lesage, R. Habchi, D. Cornu, M. Bechelany, Innovative electrospinning approach to fabricate TiO_2/NiO nanofibers for effective acetaminophen degradation, Colloids Surf. A Physicochem. Eng. Asp. 709 (2025) 136077, https://doi.org/10.1016/j.colsurfa.2024.136077.
[68] Y. Wu, M.K.Y. Chan, G. Ceder, Prediction of semiconductor band edge positions in aqueous environments from first principles, Phys. Rev. B - Condens. Matter Mater. Phys. 83 (2011) 1–7, https://doi.org/10.1103/PhysRevB.83.235301.
[69] M. Abid, I. Iatsunskyi, E. Coy, G. Lesage, A. Ben Haj Amara, M. Bechelany, Ag-BN/HNT-TiO_2 nanofibers produced by electrospinning as catalysts to remove acetaminophen, Heliyon 10 (2024) e24740, https://doi.org/10.1016/j.heliyon.2024.e24740.
[70] A. Akhundi, A. Habibi-Yan Gjeh, A simple large-scale method for preparation of g-C_3N_4/SnO_2 nanocomposite as visible-light-driven photocatalyst for degradation of an organic pollutant, Mater. Express 5 (2015) 309–318, https://doi.org/10.1166/mex.2015.1242.
[71] Y.H. Jin, C.M. Li, Y.F. Zhang, Preparation and visible-light driven photocatalytic activity of the rGO/TiO_2/BiOI heterostructure for methyl orange degradation, Xinxing Tan Cailiao/new Carbon Mater. 35 (2020) 394–400, https://doi.org/10.1016/S1872-5805(20)60496-6.
[72] H. Li, Y. Cui, W. Hong, L. Hua, D. Tao, Photodegradation of methyl orange by BiOI-sensitized TiO_2, Rare Met. 31 (2012) 604–610, https://doi.org/10.1007/s12598-012-0566-8.
[73] C.D. Wagner, NIST X-ray Photoelectron Spectrometry Database, NIST Stand. Ref. Database 20, Version 4.1. (1991) 1–76.
[74] Y. Sun, Y. Li, J. Zhan, A. Feng, C. Zhou, J. Chen, Disparate effects of four anions on the non-radical oxidation process of sulfamethoxazole by peroxymonosulfate: kinetics, mechanism and toxicity variation, J. Environ. Chem. Eng. 10 (2022) 1–9, https://doi.org/10.1016/j.jece.2022.107572.
[75] M. Jiang, J. Lu, Y. Ji, D. Kong, Bicarbonate-activated persulfate oxidation of acetaminophen, Water Res. 116 (2017) 324–331, https://doi.org/10.1016/j.watres.2017.03.043.
[76] X. Lou, C. Fang, Z. Geng, Y. Jin, D. Xiao, Z. Wang, J. Liu, Y. Guo, Significantly enhanced base activation of peroxymonosulfate by polyphosphates: Kinetics and mechanism, Chemosphere 173 (2017) 529–534, https://doi.org/10.1016/j.chemosphere.2017.01.093.
[77] G. Lente, J. Kalmár, Z. Baranyai, A. Kun, Ii. Kék, D. Bajusz, M. Takács, L. Veres, I. Fábián, One- versus two-electron oxidation with peroxomonosulfate ion: reactions with iron(II), vanadium(II), halide ions, and photoreaction with cerium (III), Inorg. Chem. 48 (2009) 1763–1773, https://doi.org/10.1021/ic801569k.
[78] S. Li, J. Li, Y. Lv, J. Ding, B. Wu, J. Zheng, H. Zhou, CeO_2 nanoparticle-modified BiOI nanoflowers as visible-light-driven heterojunction photocatalyst for tetracycline degradation and antibacterial, Mater. Today Commun. 41 (2024) 110457, https://doi.org/10.1016/j.mtcomm.2024.110457.
[79] S. Li, J. Li, Z. Sofer, L. Tao, H. Zhou, Construction of BiOI/$Bi_2Fe_4O_9$ heterojunction for visible-light-activated antibacterial: Photocatalytic sterilization of one plus one is greater than two, FlatChem 50 (2025) 100823, https://doi.org/10.1016/j.flatc.2025.100823.
[80] B. Kakavandi, M.Z. Salmasi, P. Bashardoust, S. Giannakis, R.R. Kalantary, Magnetic metal oxide catalysts: Paving the way for enhanced antibiotics degradation in wastewater via peroxymonosulfate activation, Process Saf. Environ. Prot. 182 (2024) 426–442, https://doi.org/10.1016/j.psep.2023.11.047.
[81] N. Tian, S. Giannakis, L. Akbarzadeh, F. Hasanvandian, E. Dehghanifard, B. Kakavandi, Improved catalytic performance of ZnO via coupling with $CoFe_2O_4$ and carbon nanotubes: A new, photocatalysis-mediated peroxymonosulfate activation system, applied towards Cefixime degradation, J. Environ. Manage. 329 (2023) 117022, https://doi.org/10.1016/j.jenvman.2022.117022.